




ARTICLE

# Distinct roles for luminal acidification in apical protein sorting and trafficking in zebrafish

Daniel S. Levic, Sean Ryan, Lindsay Marjoram , Jamie Honeycutt, Jennifer Bagwell , and Michel Bagnat 

**Epithelial cell physiology critically depends on the asymmetric distribution of channels and transporters. However, the mechanisms targeting membrane proteins to the apical surface are still poorly understood. Here, we performed a visual forward genetic screen in the zebrafish intestine and identified mutants with defective apical targeting of membrane proteins. One of these mutants, affecting the vacuolar H<sup>+</sup>-ATPase gene *atp6ap1b*, revealed specific requirements for luminal acidification in apical, but not basolateral, membrane protein sorting and transport. Using a low temperature block assay combined with genetic and pharmacologic perturbation of luminal pH, we monitored transport of newly synthesized membrane proteins from the TGN to apical membrane in live zebrafish. We show that vacuolar H<sup>+</sup>-ATPase activity regulates sorting of O-glycosylated proteins at the TGN, as well as Rab8-dependent post-Golgi trafficking of different classes of apical membrane proteins. Thus, luminal acidification plays distinct and specific roles in apical membrane biogenesis.**

## Introduction

Epithelial cells line the surface of most internal organs and have vital roles in physiology by mediating the transport of fluid, nutrients, and other solutes. These physiological functions are dependent on the asymmetric localization of transporters, channels, and adhesion molecules. Polarization allows cells to generate ion gradients that in turn provide the driving force for transporting sugars, amino acids, and other molecules (Caceres et al., 2017). An essential step for generating and maintaining epithelial cell polarity is the delivery of membrane proteins to the apical or basolateral plasma membrane. This process generally occurs via sorting within the TGN into distinct post-Golgi transport membrane compartments (Griffiths and Simons, 1986), followed by their trafficking along intermediate compartments and delivery to the apical or basolateral plasma membrane (Rodriguez-Boulán and Macara, 2014).

Basolateral sorting of membrane proteins has been extensively characterized (Guo et al., 2013) and involves binding of cytoplasmic adapters like clathrin to cytoplasmic sorting motifs (Fölsch et al., 1999; Gravotta et al., 2012). In contrast, the molecular mechanisms underlying apical membrane protein sorting are poorly defined. Apical sorting signals are heterogeneous and comprise luminal glycans, transmembrane domains, and/or covalently attached lipids that are inaccessible to adaptors and are not known to bind to receptors (Rodriguez-Boulán and Macara, 2014). Sorting of many apical membrane proteins depends on N- or O-glycans or protein-lipid interactions and

partitioning into lipid rafts (Brown and Rose, 1992; Scheiffele et al., 1995; Alfalah et al., 1999; Simons and Vaz, 2004; Lingwood and Simons, 2010). In other cases, glycans mediate apical sorting independently of lipid raft association (Yeaman et al., 1997; Breuza et al., 2002). This mechanism is thought to be aided by carbohydrate-binding lectins such as galectin-3 (Delacour et al., 2008), galectin-4 (Delacour et al., 2005), and galectin-9 (Mishra et al., 2010). Although mechanistically distinct, each of these modes of apical sorting involve the formation of membrane protein clusters in the TGN (Griffiths and Simons, 1986; Mellman and Simons, 1992), which facilitates segregation into apical transport carriers (Schuck and Simons, 2004; Paladino et al., 2004), and possibly also promotes carrier formation (Klemm et al., 2009). The role of clustering in protein sorting is conserved and has been implicated in plasma membrane protein sorting in budding yeast (Bagnat et al., 2000; Bagnat and Simons, 2002) and is likely also involved in apical targeting in *Caenorhabditis elegans* (Zhang et al., 2011).

Although clustering is known to promote apical sorting, the molecular machinery regulating this process in the TGN has not been identified. This raises the possibility that apical sorting is driven primarily by biophysical processes such as glycan-glycan and glycan-glycolipid interactions within the permissive acidic environment of the TGN (Hakomori, 2004; Matlin, 1986; Kim et al., 1996; Miesenböck et al., 1998). Indeed, luminal acidification was proposed decades ago to play a role in polarized sorting

Department of Cell Biology, Duke University, Durham, NC.

Correspondence to Michel Bagnat: [michel.bagnat@duke.edu](mailto:michel.bagnat@duke.edu); S. Ryan's present address is Department of Biology, St. Bonaventure University, St. Bonaventure, NY.

© 2020 Levic et al. This article is distributed under the terms of an Attribution–Noncommercial–Share Alike–No Mirror Sites license for the first six months after the publication date (see <http://www.rupress.org/terms/>). After six months it is available under a Creative Commons License (Attribution–Noncommercial–Share Alike 4.0 International license, as described at <https://creativecommons.org/licenses/by-nc-sa/4.0/>).

in epithelial cells (Matlin, 1986; Griffiths and Simons, 1986), but whether luminal pH functions in apical sorting has not been demonstrated. A recent *C. elegans* genetic screen for apical polarity identified multifaceted roles for the vacuolar H<sup>+</sup>-ATPase (V-ATPase) in brush border (BB) integrity (Bidaud-Meynard et al., 2019). However, which V-ATPase functions are attributable to its canonical role in pH regulation and how these relate to the different phases of apical protein sorting and trafficking remains unclear.

Apical trafficking networks have been extensively characterized using 2D and 3D cell culture models such as MDCK cells (Martin-Belmonte et al., 2007; Bryant et al., 2010, 2014; Apodaca et al., 2012). In vivo, clear roles for apical transport have also been identified for Rab8 (Sato et al., 2007, 2014) and Rab11 (Sobajima et al., 2014), as well as other effector proteins (Nakajo et al., 2016; Weis et al., 2016). However, the in vivo dynamics of these trafficking events and their regulation are not fully understood. One factor limiting progress in this field has been the difficulty of investigating epithelial polarization and trafficking processes in genetically tractable organisms that rely on complex sorting mechanisms, such as vertebrates.

Here, we performed a visual forward genetic screen in zebrafish to uncover factors required for apical targeting of the O-glycosylated membrane protein p75 in the intestine. Through characterization of one of these mutants, we show that luminal acidification, driven by the V-ATPase, is required for both the initial sorting and later trafficking of apical membrane proteins. By monitoring in vivo post-Golgi transport of newly synthesized membrane proteins, combined with chemical and genetic perturbation of luminal pH, we show that acidification is crucial for biosynthetic delivery of apical, but not basolateral, membrane proteins. We demonstrate that the specific requirement for H<sup>+</sup> ATPase activity in apical trafficking derives from its impact on Rab8 recruitment to tubular biosynthetic carriers.

## Results

### A forward genetic screen in zebrafish identifies regulators of apical membrane protein polarity

To uncover regulators of apical membrane biogenesis in intestinal epithelial cells (IECs), we performed a visual forward genetic screen in zebrafish using C-terminally GFP-tagged p75 (NGF receptor; Fig. 1 A) as a model apical membrane protein. This marker has been extensively characterized in cultured mammalian cells, and its apical localization has been shown to be mediated by its O-glycosylated stalk domain (Yeaman et al., 1997; Breuza et al., 2002). To monitor apical membrane protein sorting in vivo, we generated a zebrafish transgenic line, *Tg(i-fabp2:p75-GFP<sup>pd1208</sup>)*, that expresses p75-GFP in larval IECs (Fig. 1 B). In 5-d postfertilization (dpf) larvae, we observed apical enrichment (92.8% ± 1.5% of GFP signal present at the BB; Fig. 1, C and D) in IECs, with little to no intracellular localization at steady-state. We then followed a traditional 3-generation forward genetic screen using 1-ethyl-3-(3-dimethylammoniumpropyl) carbodiimide cross-linked (EMBS) mutagenesis to identify recessive mutations that impair localization of p75-GFP (Fig. 1 E). We generated 452 F2 families and screened F3 larvae at 5 dpf in ~20 clutches per family (Fig. 1 F). We first

looked for changes in p75-GFP apical membrane intensity in live larvae using a stereo microscope and then rescreened candidate mutations at higher resolution on transverse sections using confocal microscopy (Fig. 1, F-H).

From our screen, we recovered five mutants showing mislocalized p75-GFP, corresponding to four distinct phenotypic classes (Fig. 1, I-N): *cx20.16<sup>pd1215</sup>* exhibits randomized apical-basolateral missorting (Fig. 1 K, arrowheads); *bb20.14<sup>pd1216</sup>* accumulates p75-GFP in multiple small subapical vesicles (Fig. 1 L, arrows); and *bx67.16<sup>pd1217</sup>* and *bx38.22<sup>pd1218</sup>* show partial retention of p75-GFP in a highly diffuse and reticulated compartment throughout the cytoplasm (Fig. 1 M, arrows), likely the endoplasmic reticulum. The last mutant, *aa24.2<sup>pd1209</sup>*, which is the focus of these studies, is characterized by a robust intracellular accumulation of p75-GFP in enlarged subapical vacuoles (Fig. 1 N, arrows), as well as basolateral missorting (Fig. 1 N, arrowheads). We performed all our analyses at stages several days before any lethality resulting from the mutations (Fig. S1 A).

### Loss of V-ATPase function leads to intracellular accumulation of p75-GFP

To identify the mutation responsible for the *aa24.2<sup>pd1209</sup>* mutant phenotype, we used whole exome sequencing and positional cloning (Fig. 2, A and B; Ryan et al., 2013). We identified a genomic interval on chromosome 23 containing a candidate mutation affecting the splice donor site of exon 9 in *atp6ap1b* (Fig. 2 C). The mutation is predicted to cause intron readthrough and introduce a premature stop codon to the *atp6ap1b* transcript, truncating the protein before the transmembrane domain. In agreement, we detected nonsense-mediated decay of the *atp6ap1b* transcript by RT-PCR (Fig. 2 D). Rescue experiments showed that expression of WT or GFP-tagged *atp6ap1b* is sufficient to partially restore skin pigmentation, jaw morphogenesis, and body length defects of *aa24.2<sup>pd1209</sup>* mutants (Fig. S1, B, C, F, and G). Crossing the *aa24.2<sup>pd1209</sup>* allele to a previously identified *atp6ap1b* mutant allele (Nuckels et al., 2009) failed to complement these phenotypes (Fig. S1 D). Moreover, mosaic expression of HA-tagged *Atp6ap1b* in IECs suppressed p75-GFP vacuolar accumulation in *aa24.2<sup>pd1209</sup>* mutants (Fig. S1 E). These data show that loss of *atp6ap1b* causes the *aa24.2<sup>pd1209</sup>* (hereafter called *atp6ap1b<sup>pd1209</sup>*) mutant phenotype.

*Atp6ap1b* is a homologue of ATP6AP1 (aka AC45), an accessory protein subunit of the V-ATPase complex that mediates luminal acidification of both secretory and endocytic pathway organelles (Fig. 2 E; Maxson and Grinstein, 2014; Cotter et al., 2015). Consistent with a loss of V-ATPase function, *atp6ap1b<sup>pd1209</sup>* mutants showed decreased labeling of acidic compartments in the gut following gavage of the acidotropic dye LysoTracker (Fig. 2 F). To determine if the p75-GFP localization defects observed in *atp6ap1b<sup>pd1209</sup>* mutants stem from loss of V-ATPase function, we analyzed seven additional mutations affecting either the V<sub>0</sub> or V<sub>1</sub> sector of the complex (Fig. 2 G). All V-ATPase mutants analyzed exhibited subapical accumulation of p75-GFP of varying severity (Fig. 2, G and H, arrows), with some also showing basolateral missorting (Fig. 2, G and H, arrowheads). Mutants of *atp6v0ca*, which encodes the subunit comprising the

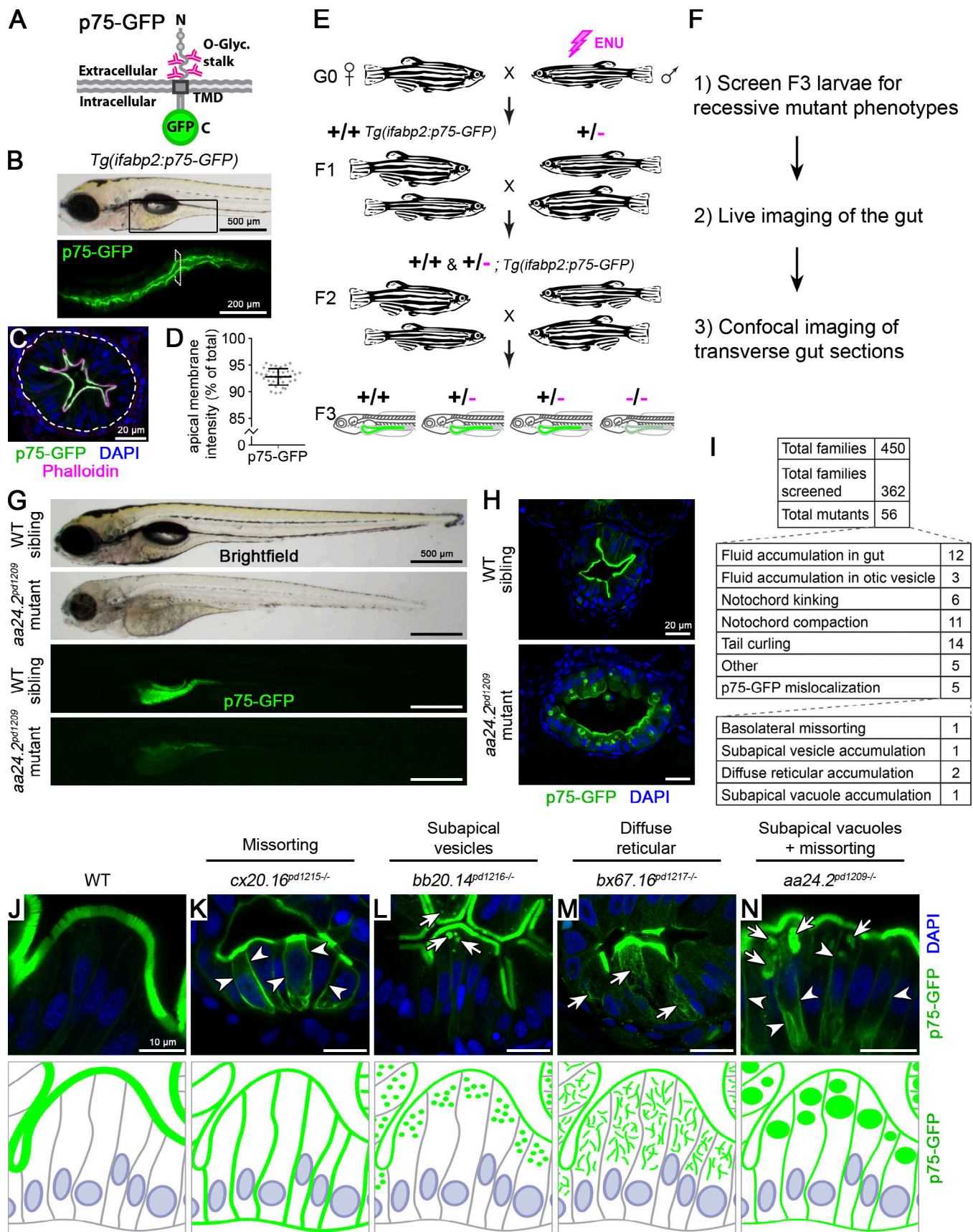


Figure 1. **Forward genetic screen identifies mutations perturbing sorting and trafficking of apical membrane proteins.** (A) Schematic of p75-GFP, a model O-glycosylated apical membrane protein. TMD, transmembrane domain. (B) *Tg(ifabp2:p75-GFP)<sup>pd1208</sup>* larvae show expression in the intestine (black box

in upper panel). **(C)** Transverse section showing p75-GFP localization at the BB. The white dotted line demarcates the intestinal epithelium. The transverse section was taken at the level indicated by the white rectangle in B. Scale bar is 20  $\mu\text{m}$ . **(D)** Quantitation of p75-GFP enrichment at the apical membrane expressed as a percentage of BB GFP signal intensity over total cellular GFP intensity.  $n = 38$  IECs from four larvae at 5 dpf. Error bars are SD. **(E)** Schematic of genetic screen design. **(F)** Workflow of screen. **(G)** Initial screen characterization of mutants. Scale bars are 500  $\mu\text{m}$ . **(H)** Confocal imaging of transverse intestinal sections. Scale bars are 20  $\mu\text{m}$ . **(I)** Mutant classes recovered from our forward genetic screen. **(J–N)** Mutants affecting p75-GFP localization. Images are representative of phenotypes observed. Arrows show intracellular accumulations; arrowheads indicate basolateral missorting. Scale bars are 10  $\mu\text{m}$ .  $n > 10$  mutants in more than three independent experiments.

proteolipid pore that transports protons, showed complete retention of p75-GFP within vacuoles and no signal at the apical membrane (Fig. 2 H). Additionally, WT larvae treated with the highly specific V-ATPase pump inhibitor bafilomycin recapitulated p75-GFP localization defects found in *atp6ap1b<sup>pd1209</sup>* mutants (Fig. 2 H). V-ATPase mutants and bafilomycin-treated larvae also showed vacuolar accumulation of p75-GFP when expressed in pronephric epithelial cells (Fig. 2, I and J, arrows), suggesting a general requirement in epithelial cells.

Together, these data show that loss of V-ATPase pump activity results in impaired apical membrane localization of p75-GFP in *atp6ap1b<sup>pd1209</sup>* mutants.

### V-ATPase function is required for polarized apical but not basolateral membrane protein delivery

To determine if localization defects in V-ATPase mutants are specific to p75-GFP, we tested other classes of polarized proteins. Similar to p75-GFP, intestinal-type sodium-phosphate cotransporter (NaPi-2b-intGFP), endogenous aminopeptidase-N (Anpep; Fig. S2), mucins, and CD36-RFP all showed vacuolar retention in *atp6ap1b<sup>pd1209</sup>* mutants (Fig. 3, A–D, arrows; and Fig. S3 A, arrows). By contrast, villin, a soluble protein highly polarized at the apical BB, did not accumulate in vacuoles (Fig. S3 B, arrows), indicating a specific defect in membrane protein transport in *atp6ap1b<sup>pd1209</sup>* mutants. In addition to subapical retention, O-glycosylated p75-GFP, Anpep, and mucins showed basolateral missorting (Fig. 3, A and C, arrowheads). Vacuolar accumulation and missorting of O-glycosylated Anpep was also observed in V-ATPase  $V_0$  and  $V_1$  sector mutants (Fig. S1 H, arrows and arrowheads, respectively).

The vacuoles containing p75-GFP were also labeled with the lysosomal marker Lamp2-RFP (Rodríguez-Fraticelli et al., 2015; Fig. 3 A, arrows). To characterize this compartment further, we collected high resolution confocal z-stacks and performed 3D rendering of Lamp2-RFP and p75-GFP. This analysis revealed a complex morphology of large vacuoles, with p75-GFP present within and surrounding the vacuoles in tubular structures (Fig. 3 E, arrows), suggesting that vacuoles fuse with apical tubular carriers that transport p75-GFP in V-ATPase mutants.

In contrast to apical membrane proteins, basolateral membrane proteins, including endogenously tagged E-cadherin-mLanYFP (Cronan and Tobin, 2019) and  $\text{Na}^+/\text{K}^+$ -ATPase, did not show vacuolar retention at steady-state in *atp6ap1b<sup>pd1209</sup>* mutants (Fig. 3, F and G, arrows). To further test whether loss of V-ATPase function specifically affects apical membrane transport, we generated heat shock-inducible lines expressing basolateral membrane proteins MICA-GFP or Aqp3-GFP, as well as apical p75-GFP (Fig. 3, H–J). We treated 5-dpf larvae for 4 h with DMSO (control) or bafilomycin immediately after heat shock induction. Although

p75-GFP accumulated subapically in vacuoles after bafilomycin treatment (Fig. 3 J, arrows), MICA-GFP and Aqp3-GFP, similar to the controls, were present at the basolateral membrane and did not accumulate intracellularly (Fig. 3, H and I).

Because the aberrant vacuoles present in *atp6ap1b<sup>pd1209</sup>* mutants sequester apical and lysosomal membrane proteins, we next asked whether cargo internalized from the apical membrane also accumulates in these vacuoles. To this end, we designed a “pulse-chase” gavage assay and followed the fate of internalized soluble cargo. Following gavage, internalization of cargo was allowed to proceed for 90 min (pulse), and then the excess cargo in the lumen was flushed with unlabeled buffer (chase), keeping the larvae in fresh water for various times before processing for analysis (Fig. S3 C). Using this approach, we observed perinuclear enrichment of endocytic tracers FM4-64 and transferrin in WT controls after a 90-min chase (Fig. S3, D and E), while *atp6ap1b<sup>pd1209</sup>* mutants accumulated the apically internalized cargo in vacuoles marked by p75-GFP (Fig. S3, D and E, arrows).

Together, these data show that loss of V-ATPase function impairs polarized trafficking of both apical N- and O-glycosylated, but not basolateral, membrane proteins, leading to their accumulation in aberrant vacuoles that also contain internalized fluid-phase cargo and lysosomal membrane proteins. Loss of V-ATPase function also causes basolateral missorting of O-glycosylated membrane proteins.

### In vivo assay of biosynthetic membrane protein trafficking

Given that *atp6ap1b<sup>pd1209</sup>* mutants accumulate cargo internalized from the apical surface within vacuoles, it was unclear whether retention of apical membrane proteins in these mutants occurs primarily during biosynthetic transport or due to impaired recycling following endocytosis.

To distinguish between these two possibilities, we developed an in vivo assay based on the low temperature block and release of biosynthetic cargo transport at the TGN. This assay originated from the discovery that cargo export from the TGN is naturally temperature sensitive and can be temporarily and reversibly blocked by incubating mammalian cells at 20°C for several hours and then shifting them back to 37°C (Matlin and Simons, 1983). By combining a low temperature block with selective labeling of newly synthesized proteins (e.g., pulse-chase radiolabeling), it was possible to monitor biosynthetic TGN export of a cohort of labeled membrane proteins. To adapt this assay for an in vivo microscopy setting, we used our inducible p75-GFP line and found a temperature that blocks transport of newly synthesized p75-GFP with no deleterious effects and complete recovery after returning the larvae to the physiological temperature. We found that incubation of 5-dpf larvae at 14°C for 2 h immediately after a

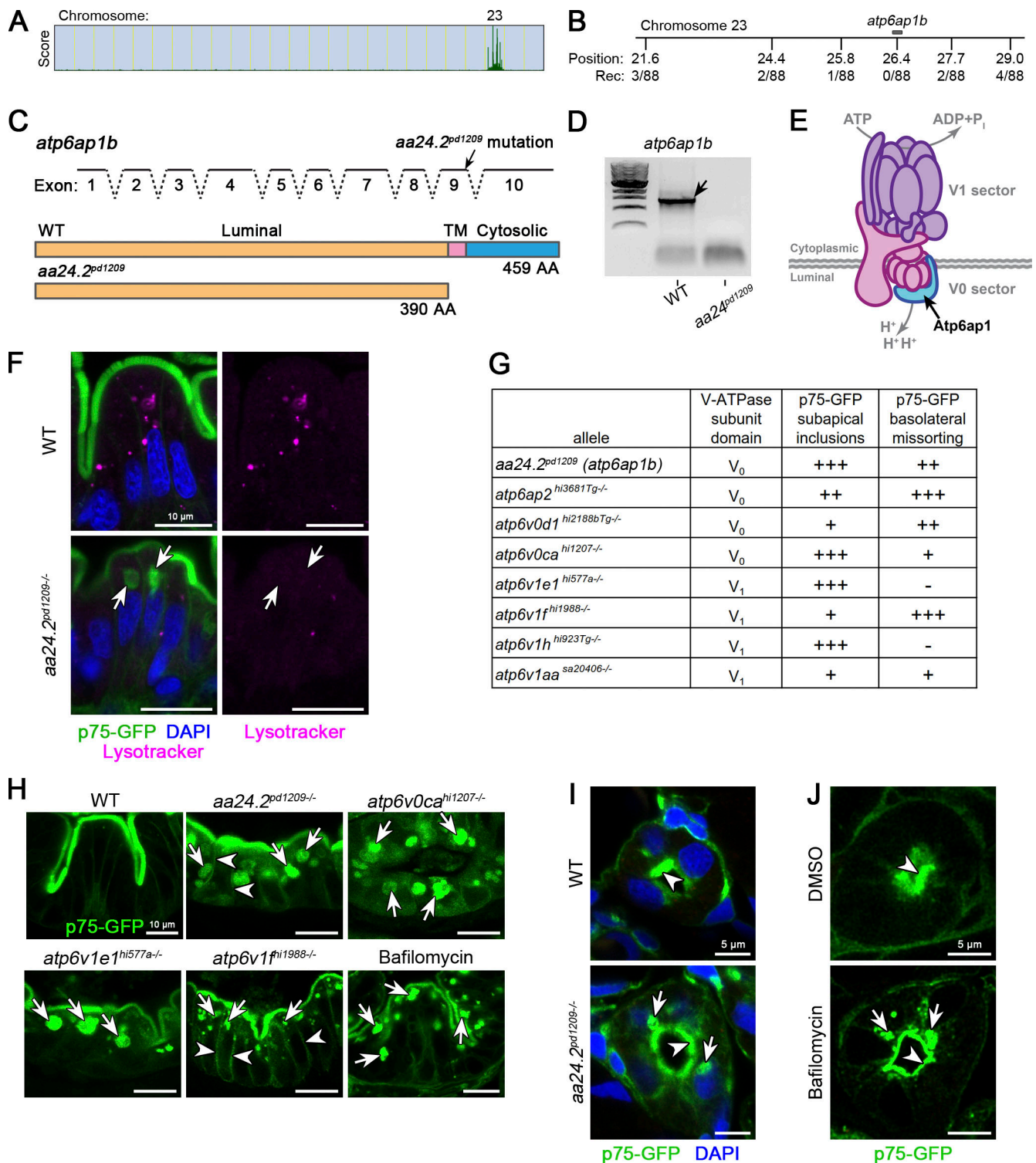


**Figure 2. V-ATPase function is required for apical membrane protein delivery.** (A–D) Identification of *aa24.2<sup>pd1209</sup>* as a splice site mutation in *atp6ap1b* of the V-ATPase complex. SNPtrack linkage analysis (A) and positional cloning (B) of the *aa24.2<sup>pd1209</sup>* mutation affecting the splice donor site of exon 9 of *atp6ap1b* (C). Rec, recombinants; TM, transmembrane. (D) RT-PCR showing decay of the *atp6ap1b* mutated transcript. (E) Illustration of the V-ATPase complex. (F) *aa24.2<sup>pd1209</sup>* mutants show decreased labeling of acidic organelles; aberrant vacuoles are not acidified (arrows). Larvae were gavaged with LysoTracker and processed within 30 min for confocal microscopy. *n* = 8 mutants in three independent experiments. (G and H) All V-ATPase subunits analyzed showed variable defects in apical membrane protein trafficking and sorting. (G) Genetic analysis of V-ATPase subunit mutants. Plus signs indicate relative penetrance for each phenotype. (H) p75-GFP localization in different V<sub>0</sub> and V<sub>1</sub> sector V-ATPase mutants. Arrows point to vacuolar accumulation; arrowheads show basolateral missorting. *n* > 10 larvae of each genotype/treatment from at least two independent experiments. Scale bars are 10 μm. (I and J) p75-GFP localization in the pronephros of *aa24.2<sup>pd1209</sup>* mutants and bafilomycin-treated larvae. *n* > 3 larvae of each genotype/treatment from at least two independent experiments. Scale bars are 5 μm.

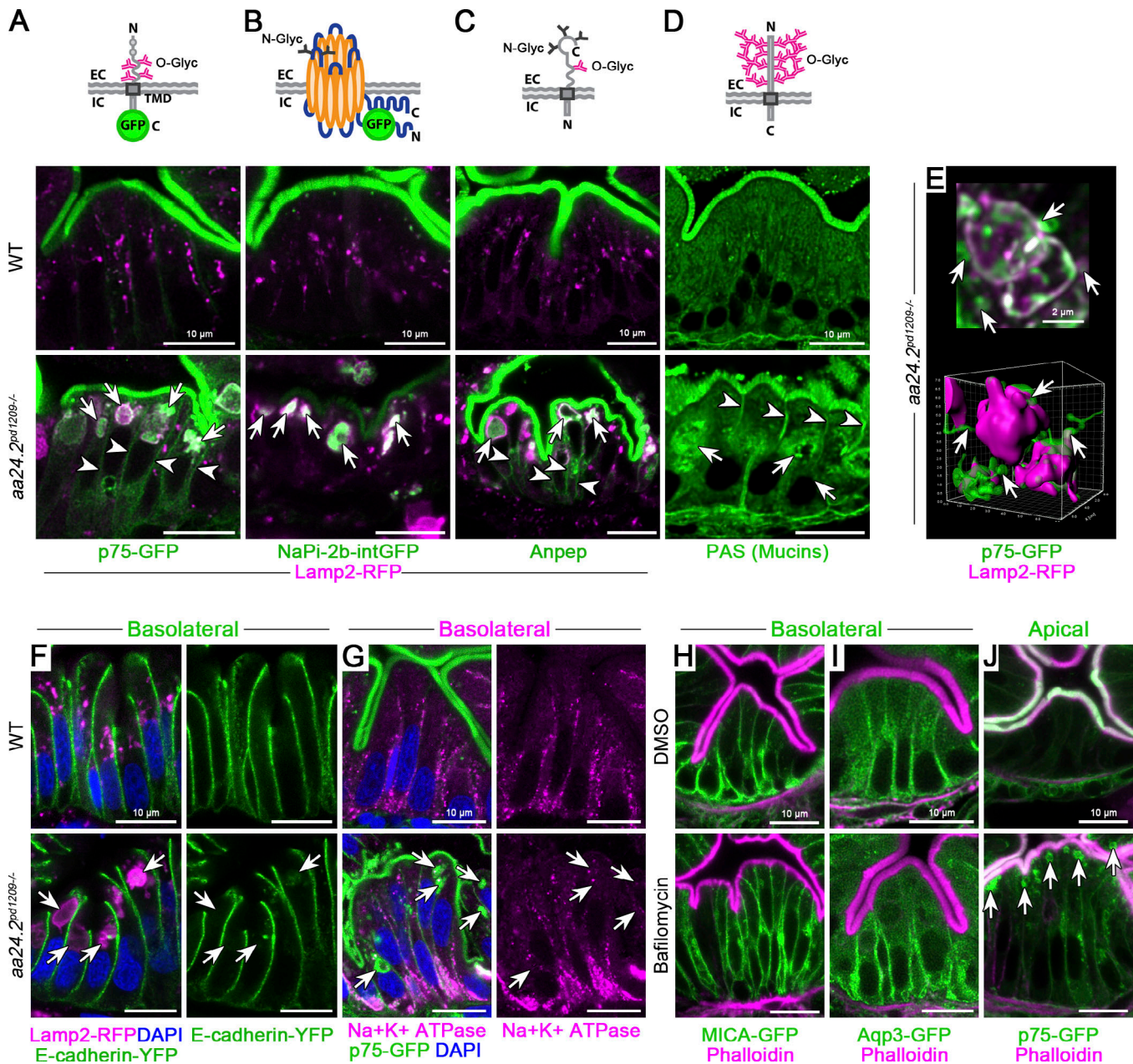


**Figure 3. Loss of V-ATPase function impairs apical but not basolateral membrane protein delivery.** (A–D) Schematic and localization of O- and N-glycosylated apical membrane proteins in *aa24.2<sup>pd1209-/-</sup>* mutants. Mutants retain apical membrane proteins in aberrant apical vacuoles, marked with Lamp2-RFP. Arrows point to vacuoles; arrowheads to basolateral missorting.  $n \geq 7$  mutants in at least two independent clutches for A–C;  $n = 3$  mutants for D. Scale bars are 10  $\mu$ m. C, C-terminus; EC, extracellular; Glyc, glycan; IC, intracellular; N, N-terminus; TMD, transmembrane domain. (E) 0.6- $\mu$ m depth 2D projection (two optical slices) of p75-GFP/Lamp2-RFP vacuoles (top) and corresponding 7.2- $\mu$ m depth 3D reconstruction (bottom). p75-GFP shows a tubular appearance in addition to vacuolar retention in *aa24.2<sup>pd1209-/-</sup>* mutants (arrows). Data are from z-series taken for experiments in A. Scale bars are 2  $\mu$ m. (F–J) Basolateral membrane proteins are not retained in vacuoles (arrows) upon loss of V-ATPase function. Endogenously expressed E-cadherin-YFP (F) and Na<sup>+</sup>K<sup>+</sup> ATPase (G) do not accumulate in vacuoles in *aa24.2<sup>pd1209-/-</sup>* mutants.  $n > 10$  mutants from three independent experiments for F and G. Overexpressed MICA-GFP (H) and Aqp3-GFP (I) do not accumulate intracellularly, as with p75-GFP (J), in larvae treated with 500 nM bafilomycin for 4 h.  $n \geq 6$  larvae per condition for H–J. Scale bars are 10  $\mu$ m.

30-min 42°C heat shock induction can serve as an effective and well-tolerated (100% survival) temperature block for p75-GFP (Fig. 4 A). Larvae subjected to these conditions showed perinuclear accumulation of p75-GFP, whereas incubation at the physiological temperature of 28°C for the same duration led to apical membrane enrichment (Fig. 4, B and C, arrows). Using

B4GALT1-tagRFP as a marker for the TGN, we found that p75-GFP accumulated in the TGN of enterocytes (Fig. 4, D and E), as is the case for cultured mammalian cells in the classic 20°C TGN block (Matlin and Simons, 1983).

Next, to monitor biosynthetic post-Golgi transport, we performed a low temperature block and then shifted the larvae back

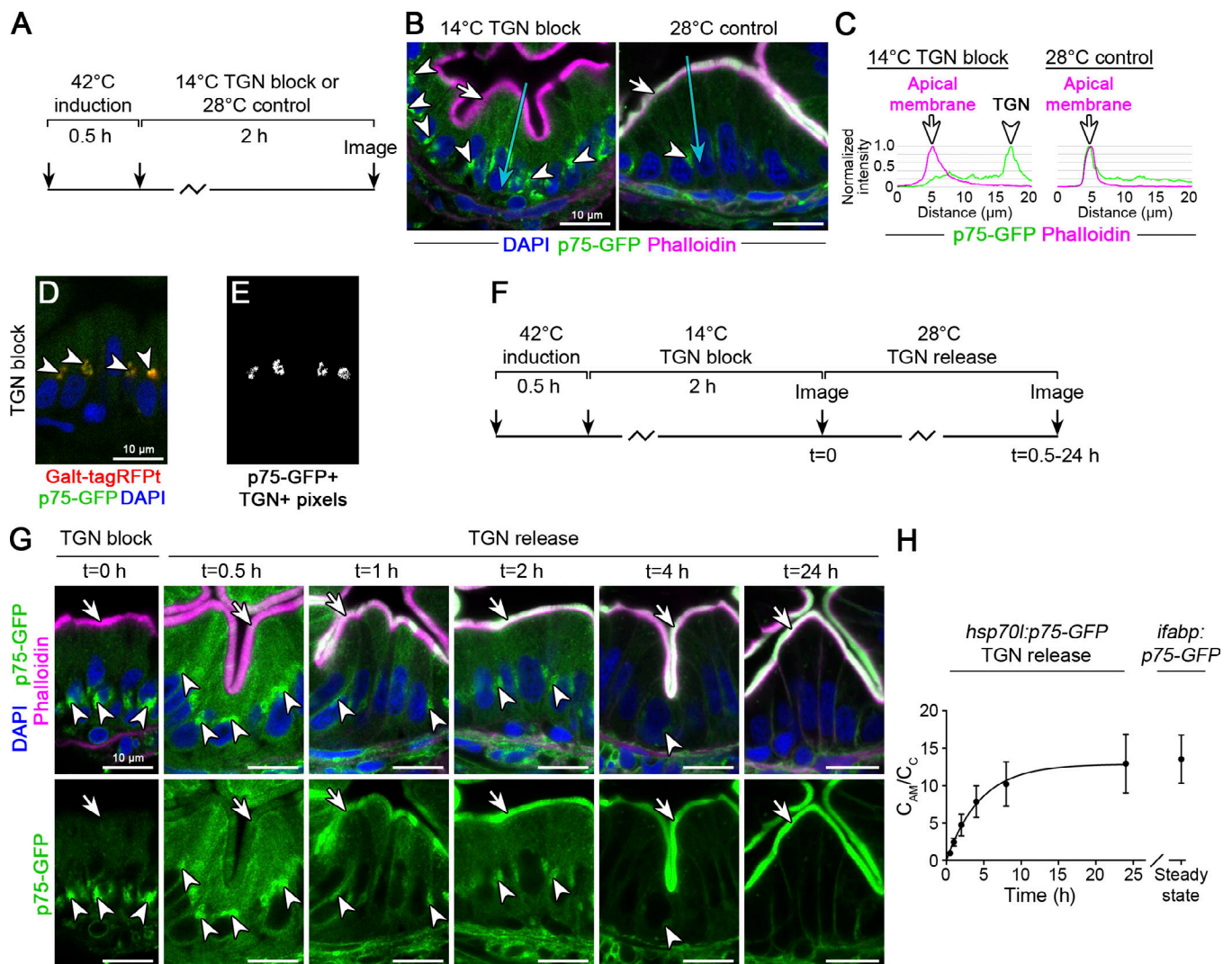


**Figure 4. A low temperature block synchronizes biosynthetic transport of p75 in the TGN in vivo. (A–E)** A low temperature TGN block for zebrafish larvae. **(A)** Schematic of low-temperature TGN block. **(B and C)** Apical membrane transport (arrow) of newly synthesized p75-GFP is stalled after a 2-h low temperature block. Arrowheads point to perinuclear pool.  $n \geq 5$  larvae per condition in three independent experiments. Scale bars are 10  $\mu\text{m}$ . **(D)** Newly synthesized p75-GFP is retained at the TGN (arrowheads), marked by Galt-tagRFPT.  $n = 5$  larvae. **(E)** Colocalized p75-GFP+ and B4GALT1-tagRFPT+ pixels from D. Scale bars are 10  $\mu\text{m}$ . **(F–H)** A TGN block and release assay for zebrafish larvae. **(F)** Experimental strategy. **(G)** p75-GFP localization at various time points after a TGN release. p75-GFP is rapidly released from the TGN into apical carriers, progressively accumulating at the apical membrane. Scale bars are 10  $\mu\text{m}$ . **(H)** Kinetic analysis of p75-GFP transport after a TGN release plotted as a ratio of apical membrane intensity ( $C_{AM}$ ) to cytoplasm intensity ( $C_C$ ) over time. Data are fitted with a one-phase exponential association model ( $R^2 = 0.8159$ ;  $n > 20$  cells from at least two animals per time point; error bars are SD).

to their physiological 28°C temperature to release p75-GFP from the TGN and imaged the intestine after defined time intervals (Fig. 4 F). p75-GFP rapidly exited the TGN (Fig. 4 G, arrowheads) in apical carriers and began to populate the BB (Fig. 4 G, arrows) within 1 h of TGN release. Between 1–4 h of TGN release, p75-GFP was depleted from the TGN and became enriched at the apical membrane (Fig. 4 G, arrows), reaching steady-state localization within ~8 h after TGN release, with the signal remaining stable at the apical membrane for  $\geq 24$  h (Fig. 4 H).

#### V-ATPase activity is required for the biosynthetic transport of p75-GFP

At steady-state, V-ATPase mutants show progressive accumulation of apical membrane proteins in aberrant vacuoles

between 3–5 dpf (Fig. 5 A, arrows). To determine how V-ATPase function regulates apical membrane protein trafficking during distinct steps of transport, we monitored p75-GFP localization after a TGN release in the presence of DMSO (control) or bafilomycin to inhibit V-ATPase H<sup>+</sup> pump activity (Fig. 5 B). 1 h following TGN release, control larvae showed a clear enrichment of p75-GFP at the apical membrane (Fig. 5 C and D, arrows). By contrast, bafilomycin-treated larvae showed p75-GFP accumulation subapically (Fig. 5 C, arrowheads), with only a minor pool present at the apical membrane (Fig. 5 D, arrow). Perinuclear localization of p75-GFP was also more prominent in bafilomycin-treated larvae, suggesting a potential role for V-ATPase activity at the TGN (Fig. 5 C). After a 4-h TGN release, p75-GFP largely remained accumulated subapically in bafilomycin-treated larvae

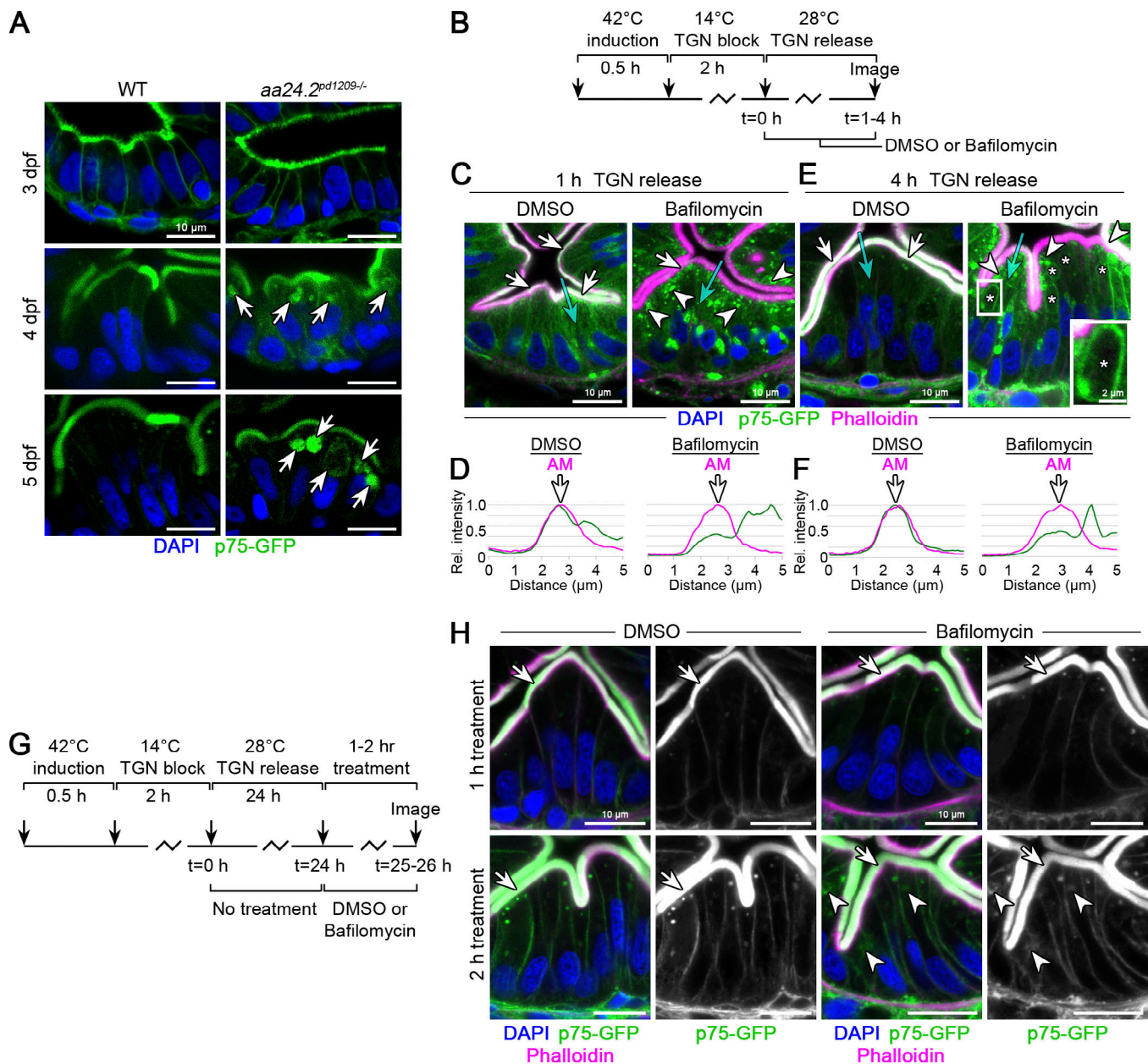


**Figure 5. V-ATPase activity is required for biosynthetic delivery of apical membrane proteins. (A)** p75-GFP localization in the gut of *aa24.2<sup>pd1209-/-</sup>* mutants at 3–5 dpf. Arrows point to intracellular accumulation.  $n \geq 5$  larvae per genotype per stage. Scale bars are 10 μm. **(B)** Experimental strategy for a 1- or 4-h TGN release in the presence of 750 nM bafilomycin or DMSO. **(C)** p75-GFP surface delivery (arrows) is blocked by bafilomycin, leading to subapical accumulation (arrowheads).  $n = 6$  for bafilomycin and 4 for DMSO. Scale bars are 10 μm. **(D)** Line profiles of p75-GFP from the cyan arrows in C. Phalloidin marks the BB. Rel., relative. **(E)** p75-GFP accumulates in apical vacuoles within 4 h of TGN release with bafilomycin. Arrows point to the apical membrane; arrowheads to subapical accumulation; asterisks mark vacuoles.  $n = 6$  for bafilomycin and 3 for controls. Scale bars are 10 μm and 2 μm (white box). **(F)** Line profiles of p75-GFP from the cyan arrows in E. **(G)** Experimental design. p75-GFP was allowed to reach steady-state accumulation at the apical membrane by a 24-h TGN release. Then, 750 nM bafilomycin or DMSO was applied for 1 or 2 h, and larvae were processed for imaging. **(H)** No apical membrane localization (arrows) or subapical accumulation were observed after 1 h of bafilomycin treatment. Only sparse subapical accumulations (arrowheads) were seen after 2 h of bafilomycin treatment. At least five bafilomycin-treated larvae and at least four controls were imaged per time point. Scale bars are 10 μm.

(Fig. 5 E, arrowheads), was depleted at the apical membrane (Fig. 5, E and F, arrows), and began to line vacuolar compartments similar to those present in V-ATPase mutants (Fig. 5 E, asterisks, inset).

To determine whether the observed trafficking defects were of biosynthetic origin, we modified our TGN release assay to distinguish between biosynthetic transport and the recycling

pathway. We first allowed p75-GFP to reach steady-state localization at the apical membrane with a 24-h TGN release and then applied bafilomycin for 1–2 h (Fig. 5 G). With this pulse-chase approach, no additional synthesis of p75-GFP occurs during the bafilomycin treatment, and any accumulation subapically would have to result from apical membrane recycling. Under these conditions, apical p75-GFP localization was largely unaffected,



and only a small subapical pool, likely representing recycling compartments, could be detected upon bafilomycin treatment (Fig. 5 H, arrowheads).

Together, these data indicate that loss of V-ATPase function impairs biosynthetic trafficking of newly synthesized p75-GFP to the apical membrane.

### Distinct roles for V-ATPase-dependent luminal acidification in apical membrane protein sorting and trafficking

In the course of our study, we noted that inhibiting V-ATPase activity appeared to delay export of p75-GFP from the TGN after a 1-h release (Fig. 5 C). The TGN was shown to be a critical sorting compartment for membrane proteins in mammalian cells and yeast (Wandinger-Ness et al., 1990; Keller et al., 2001; Klemm et al., 2009). Although luminal pH was postulated to influence protein sorting in epithelial cells (Matlin, 1986; Griffiths and Simons, 1986), a role for V-ATPase activity in this context has not been explored. Given our data showing that V-ATPase mutants exhibited missorting of O-glycosylated apical membrane proteins (Fig. 2 and Fig. 3), we hypothesized that luminal acidification of the TGN is required for proper sorting. To test this possibility, we turned to agents that neutralize luminal pH independently of the V-ATPase (Fig. 6 A).

Luminal pH depends not only on activity of the V-ATPase, but also on transporters that use H<sup>+</sup> gradients to transport other ions, such as Na<sup>+</sup>/H<sup>+</sup> exchangers (Orlowski and Grinstein, 2011; Casey et al., 2010). Although bafilomycin inhibits H<sup>+</sup> pump activity, its effect on luminal pH is relatively slow as it depends on H<sup>+</sup> transport through other transporters (Poëa-Guyon et al., 2013; Casey et al., 2010). Furthermore, different organelles exhibit distinct H<sup>+</sup> leakage kinetics (Wu et al., 2001), confounding functional analysis of luminal pH based exclusively on pump inhibitors. Ionophores, on the other hand, rapidly neutralize luminal pH within minutes by sequestering specific cations, thereby hyperactivating H<sup>+</sup> export through exchangers (Fig. 6 A; Poëa-Guyon et al., 2013). This is an important distinction because when we inhibit H<sup>+</sup> pump activity with bafilomycin immediately following TGN release, the relatively slow kinetics of pH neutralization may hinder our ability to test how alkalinization of the TGN influences apical sorting of p75-GFP, which rapidly exits upon TGN release (Fig. 4, G and H).

To determine the extent to which ionophore/inhibitor treatments alter TGN luminal pH in IECs, we generated a line expressing a TGN-localized ratiometric pH sensor, consisting of the N-terminus and transmembrane domain of B4GALT1 (Qasba et al., 2008), and tagged in its luminal domain with pH-sensitive se-pHluorin (Sankaranarayanan et al., 2000) and pH-insensitive tagRFPT (Shaner et al., 2008; Fig. S4 A). We first generated a standard curve by incubating intestinal sections obtained from larvae expressing the sensor in pH-calibrated buffers and measuring se-pHluorin/tagRFPT intensity ratios with defined confocal imaging parameters (Fig. S4, B and C). Next, we treated larvae with DMSO (control), bafilomycin, or ionophores and performed live imaging of the TGN pH sensor in IECs 2 h later using identical imaging specifications as for standard curve analysis to extrapolate absolute pH values. Control larvae showed an average TGN luminal pH of ~6.4 (Fig. S4, D and E),

which is in line with values reported for the TGN with other pH sensors in cultured mammalian cells (Kim et al., 1996; Miesenböck et al., 1998; Maeda et al., 2008; Hummer et al., 2017). Treatment with bafilomycin or ionophores (monensin or nigericin) alkalinized TGN pH. However, the Na<sup>+</sup> selective ionophore monensin exerted a much stronger effect than the K<sup>+</sup> selective ionophore nigericin (Fig. S4 E), possibly reflecting differential abundance or activity of H<sup>+</sup> exchangers that use these cations in the TGN in IECs.

Next, we tested how TGN luminal acidification affected apical membrane protein transport. We performed a TGN release and immediately gavaged either DMSO (control), bafilomycin, monensin, or ammonium, and then followed p75-GFP localization 1 h later (Fig. 6 B). As before, bafilomycin treatment resulted in subapical accumulation of p75-GFP (Fig. 6 C, arrows). By contrast, ionophore or ammonium treatment resulted in robust basolateral missorting of p75-GFP (Fig. 6 C, arrowheads). Subapical accumulations were present after ionophore gavage, but they were less prominent than with bafilomycin treatment (Fig. 6 C, arrows), likely due to a large fraction of p75-GFP being rerouted basolaterally before reaching apical carriers. Accordingly, when we pretreated larvae with bafilomycin by gavage to allow for pH neutralization before induction of p75-GFP (Fig. 6 D), p75-GFP showed robust basolateral missorting (Fig. 6 E, arrowheads) and less prominent apical accumulation (Fig. 6 E, arrows), similar to the more rapid effect of ionophore treatment (Fig. 6 C, arrowheads). Basolateral missorting of p75-GFP did not appear to stem from changes in its post-translational processing as no obvious defects could be detected by immunoprecipitation (IP) and Western blotting (Fig. S4, F and G, arrowheads).

To determine if luminal acidification similarly regulates transport of membrane proteins other than p75-GFP, we performed a 2-h TGN release experiment in the presence of DMSO (control), bafilomycin, or monensin (Fig. 7 A) in larvae expressing different classes of polarized membrane proteins (Fig. 7 B). We tested the multipass apical N-glycosylated CD36-GFP (a fatty acid transporter) and apical NaPi-2b-intGFP, as well as the basolateral protein MICA-GFP, which is also N-glycosylated but harbors a dominant dihydrophobic sorting motif (Suemizu et al., 2002; Fig. 7 B). In controls, each of the polarized membrane proteins were efficiently delivered to the apical or basolateral plasma membrane within 2 h of TGN release, as typically found in WT under normal conditions (Fig. 7, C-F). Bafilomycin treatment led to subapical accumulation of the apical membrane proteins p75-GFP, CD36-GFP, and NaPi-2b-intGFP (Fig. 7, G-I, arrows). Interestingly, although O-glycosylated p75-GFP showed basolateral missorting after monensin treatment (Fig. 7 K), N-glycosylated CD36-GFP and NaPi-2b-intGFP exhibited subapical accumulation, but without basolateral missorting (Fig. 7, L and M). Under these conditions, MICA-GFP remained unaffected by either treatment and was properly sorted to the basolateral membrane (Fig. 7, J and N), showing only a small intracellular pool after bafilomycin treatment, likely resulting from impaired recycling (Fig. S5 E). These data are consistent with our genetic analysis showing that V-ATPase mutants missort apical O-glycosylated p75-GFP, aminopeptidase, and mucins to the basolateral membrane (Fig. 2 H and Fig. 3, A, C, and D) but not

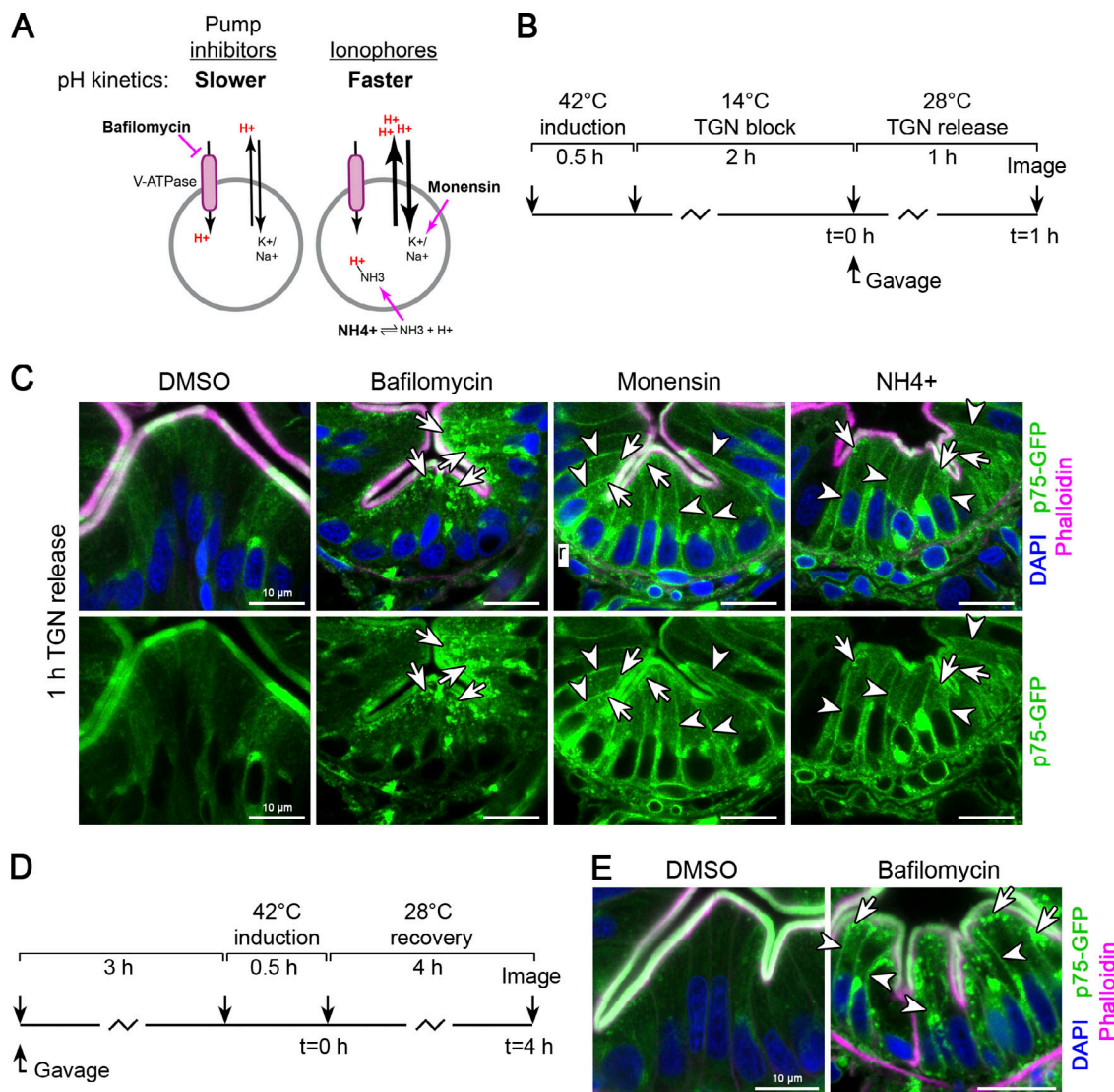


**Figure 6. Luminal acidification is required for distinct steps of apical membrane protein sorting and trafficking.** (A) Schematic (adapted and reprinted with permission from the *Journal of Cell Biology*; Poëa-Guyon et al., 2013) of the mechanisms of action and luminal pH kinetics of V-ATPase inhibitors versus ionophores. (B) Experimental strategy. Immediately upon TGN release, larvae were gavaged with DMSO, 500 nM bafilomycin, 25 μM monensin, or 100 mM NH<sub>4</sub>Cl, immersed in the same compound, and processed for imaging 1 h later. (C) Ionophore treatment results in apical-basolateral missorting (arrowheads), while bafilomycin treatment leads to subapical accumulation (arrows) after a 1 h TGN release. *n* ≥ 5 larvae per condition in two independent experiments. Scale bars are 10 μm. (D) Experimental strategy. The intestines of larvae were pretreated with bafilomycin by gavage before p75-GFP induction. After induction, larvae were immersed in bafilomycin and processed for imaging at time points indicated. (E) p75-GFP exhibits apical-basolateral missorting when bafilomycin is applied before its expression and sorting. Arrowheads point to basolateral missorting; arrows point to apical accumulation. *n* ≥ 8 larvae per condition in two independent experiments. Scale bars are 10 μm.

N-glycosylated NaPi-2b-intGFP (Fig. 3 B), which only accumulates subapically.

Together, these data reveal that luminal acidification of post-Golgi carriers is broadly required for biosynthetic trafficking of apical, but not basolateral, membrane proteins and that TGN luminal acidification is specifically required for proper sorting of O-glycosylated apical membrane proteins.

#### Loss of V-ATPase activity leads to acute collapse of Rab8<sup>+</sup> tubules into vacuoles that recruit apical carriers

To characterize the apical carriers that transport p75-GFP *in vivo*, we followed its localization in larvae expressing

mRFP-Rab8a, a GTPase known to regulate apical trafficking in IECs (Sato et al., 2007, 2014; Nakajo et al., 2016). After a 1-h TGN release, p75-GFP overlapped with Rab8a in post-Golgi tubules (Fig. 8, A and B, arrowheads), as well as within small apical carriers at the terminal web, close to the BB (Fig. 8, A and B, arrows). Super-resolution stimulated emission depletion (STED) microscopy confirmed that p75-GFP closely overlapped with Rab8<sup>+</sup> tubules during biosynthetic transport (Fig. 8, C-F). Additionally, mRFP-Rab8a marked tubules near the basolateral membrane that were devoid of p75-GFP (Fig. 8, C and D). Live *in vivo* imaging shortly after a TGN release revealed p75-GFP exiting the TGN along dynamic mRFP-Rab8a tubules (Fig. 8 G,

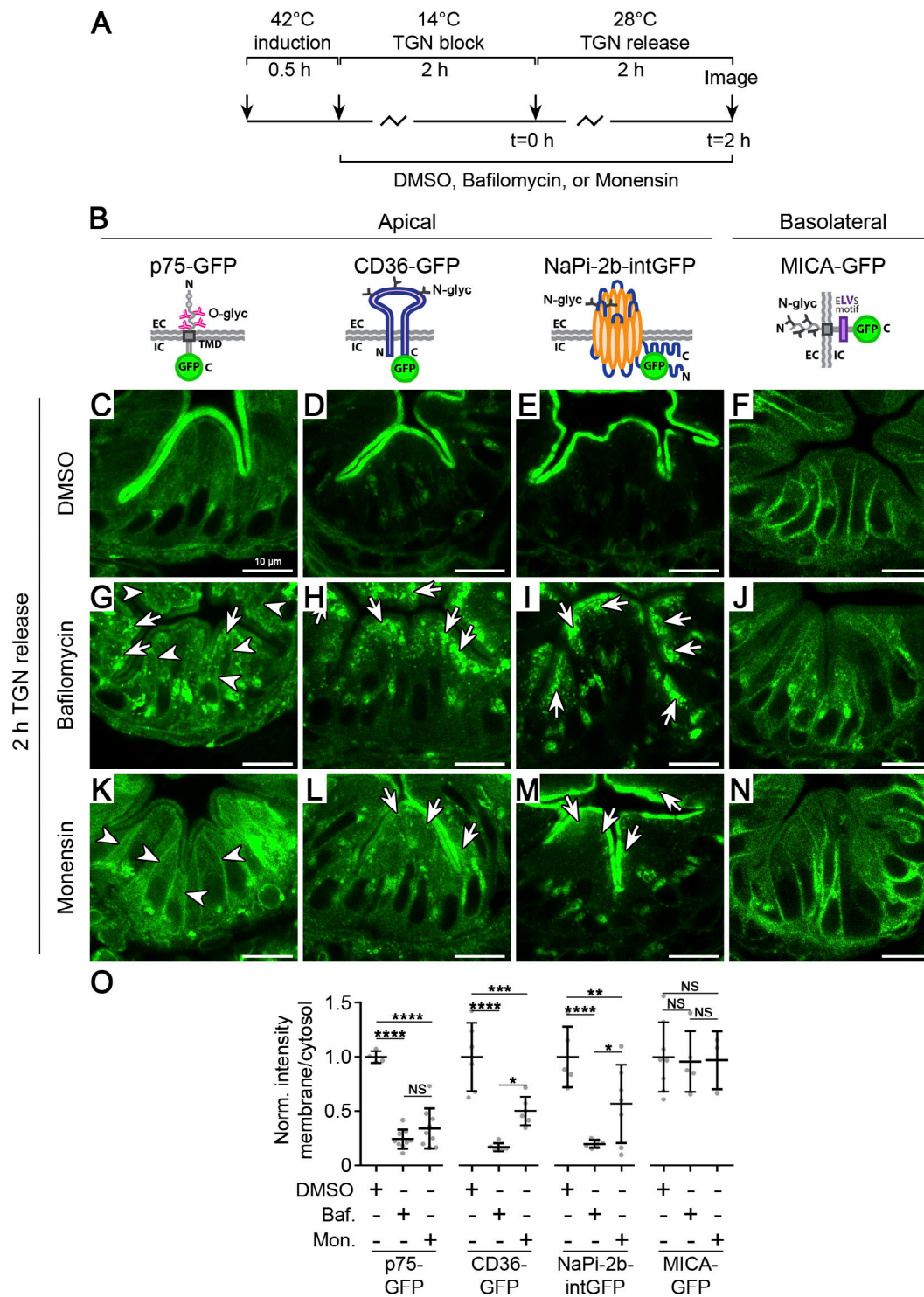


**Figure 7. Differential requirements of luminal acidification for sorting and trafficking of membrane proteins.** (A) Experimental strategy. After transgene induction, larvae were treated with DMSO, 750 nM bafilomycin, or 25 μM monensin and then subjected to a TGN block and 2-h release. (B) Illustrations of different classes of polarized membrane proteins. C, C-terminus; glyc, glycan; N, N-terminus; TMD, transmembrane domain. (C–F) Under control conditions (DMSO), each membrane protein is enriched at the cell surface after a 2-h TGN release. Scale bars are 10 μm. (G–J) After bafilomycin treatment, apical membrane proteins p75-GFP, CD36-GFP, and NaPi-2b-intGFP accumulate subapically (arrows), while basolateral membrane protein MICA-GFP does not accumulate comparably. Scale bars are 10 μm. (K–N) After monensin treatment, the O-glycosylated apical membrane protein p75-GFP is basolaterally missorted (arrowheads), the N-glycosylated apical membrane proteins CD36-GFP and NaPi-2b-intGFP accumulate subapically (arrows), and the N-glycosylated basolateral membrane protein MICA-GFP is relatively unaffected. Scale bars are 10 μm. (O) Quantification of intracellular accumulation expressed as a ratio of mean apical membrane intensity to cytoplasm intensity. Data were normalized to DMSO controls, and each data point is an individual larva.  $n \geq 3$  larvae per condition representing  $\geq 20$  cells. Error bars are SD. \*\*\*\*,  $P < 0.0001$ ; \*\*\*,  $P < 0.001$ ; \*\*,  $P < 0.01$ ; \*,  $P < 0.05$ . Baf., bafilomycin; EC, extracellular; IC, intracellular; Mon., monensin; Norm., normal. Two-way ANOVA with Tukey’s multiple comparison test.

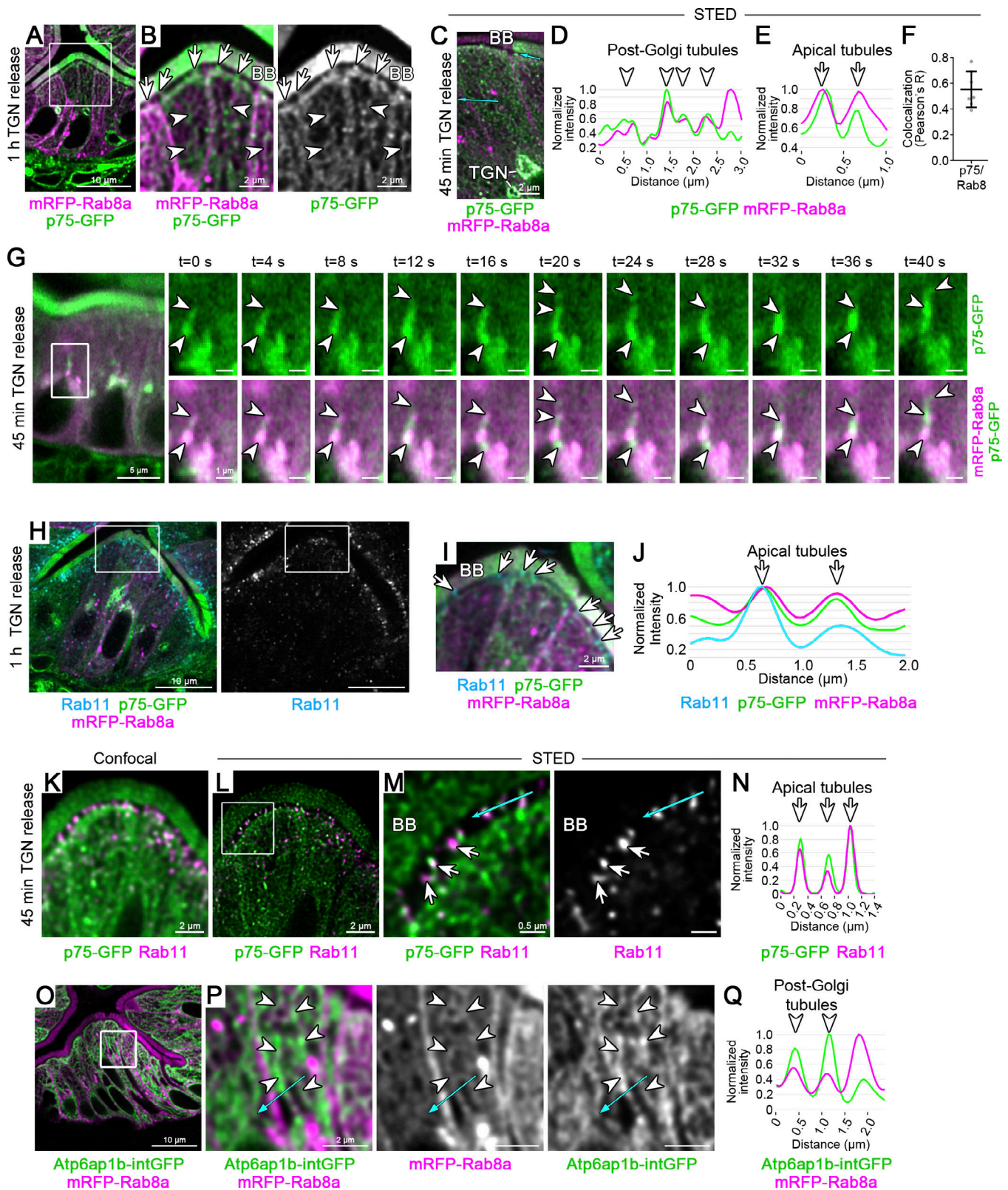


Figure 8. **Biosynthetic transport of p75 through distinct tubular carriers en route to the apical membrane.** (A–C) p75-GFP is present in post-Golgi Rab8 tubules during biosynthetic transport. (A) p75-GFP was imaged in *Tg(cldn15la:qf2)<sup>pd1142</sup>;Tg(quas:mRFP-Rab8a)<sup>pd1213</sup>* larvae (mRFP-Rab8a expressing larvae) after a 1-h TGN release.  $n \geq 4$  larvae per condition in two independent experiments. Scale bar is 10  $\mu\text{m}$ . (B) Magnified insets of A. p75-GFP is present in post-Golgi tubules (arrowheads) and apical tubules (arrows) at the terminal web, marked by mRFP-Rab8a, as well as the BB. Scale bars are 2  $\mu\text{m}$ . (C–F) p75-GFP colocalizes with mRFP-Rab8a in tubular carriers. (C) p75-GFP was imaged after a 1-h TGN release in mRFP-Rab8a expressing larvae, labeled with anti-GFP-ATTO647 and anti-RFP-STAR580, and imaged with STED microscopy. Scale bar is 1  $\mu\text{m}$ . Cyan arrows indicate line profiles (D and E). (F) p75-GFP colocalization

with mRFP-Rab8.  $n = 7$  larvae representing 22 ROIs of the apical cytoplasm. Error bars are SD. **(G)** p75-GFP was live-imaged in the intestine of mRFP-Rab8a expressing larvae after a 45-min TGN release using Airyscan. Arrowheads point to p75<sup>+</sup>/Rab8<sup>+</sup> tubules extending from the region of the TGN.  $n = 10$  larvae. Scale bars are 5  $\mu\text{m}$  in left panel and 1  $\mu\text{m}$  in magnified insets. See also [Video 1](#). **(H–N)** p75/Rab8a apical tubules overlap with Rab11. **(H)** p75-GFP was imaged in mRFP-Rab8a expressing larvae after a 1-h TGN release and stained for endogenous Rab11.  $n = 9$  larvae. Scale bars are 10  $\mu\text{m}$ . **(I)** Magnified inset of G. Arrows indicate apical tubules at the terminal web. Scale bar is 2  $\mu\text{m}$ . **(J)** Line profile showing overlap of p75, Rab8a, and Rab11 at apical tubules (arrows) from H. **(K–M)** Confocal (K) and STED (L and M) imaging of Rab11-AF594 and p75-GFP-ATTO647 localization at apical tubules after a 1-h TGN release.  $n = 10$  larvae. **(M)** Magnified inset of K showing colocalization of p75-GFP with Rab11 in apical tubules at the terminal web. Cyan line indicates line profile in N. Scale bars are 2  $\mu\text{m}$  (K and L) or 0.5  $\mu\text{m}$  (M). **(O–Q)** V-ATPase, marked by Atp6ap1b-intGFP, overlaps with post-Golgi Rab8 tubules. **(O)** Localization of Rab8a and Atp6ap1b-GFP.  $n = 11$  larvae. Scale bar is 10  $\mu\text{m}$ . **(P)** Magnified insets of N. Atp6ap1b-intGFP is present in mRFP-Rab8a tubules (arrows). Scale bars are 2  $\mu\text{m}$ . Cyan arrow indicates line profile in Q.

arrowheads; and [Video 1](#), white rectangles). On the other hand, Rab11, a GTPase implicated in apical trafficking ([Bryant et al., 2010](#); [Knowles et al., 2015](#); [Sobajima et al., 2014](#)), was absent from elongated post-Golgi tubules and was instead enriched at apical terminal web structures along with mRFP-Rab8a and p75-GFP after a 1-h TGN release ([Fig. 8, H–J](#)). Overexpressed GFP-Rab11a was similarly enriched apically but absent from post-Golgi tubules (data not shown). STED imaging revealed that these apical Rab11a structures consisted of small tubules projecting from subapical networks through the terminal web and to the BB ([Fig. 8, K–N](#)). Because these tubules appeared to connect apical tubular networks toward the BB, terminal web Rab8/Rab11<sup>+</sup> tubules may represent the last transport compartment responsible for membrane protein delivery to the apical plasma membrane. Accordingly, after a short TGN release, we often observed p75-GFP highly enriched at apical membrane subdomains directly adjacent to apical p75<sup>+</sup>/Rab8<sup>+</sup> tubules ([Fig. 9 A](#), top: panels, arrows and overlying BB).

To determine if biosynthetic apical carriers also harbor V-ATPase subunits, we generated a transgenic line expressing Atp6ap1b internally tagged with GFP in the middle of its luminal domain (Atp6ap1b-intGFP), which we found was able to partially rescue *atp6ap1b*<sup>pd209</sup> mutants ([Fig. S1, F and G](#)). Atp6ap1b-intGFP overlapped with mRFP-Rab8a in post-Golgi tubules ([Fig. 8, O–Q](#), arrowheads), as well as with the V-ATPase c subunit Atp6v0ca-mScarlet (data not shown). Together, these data indicate that post-Golgi Rab8<sup>+</sup> tubules and apical Rab11<sup>+</sup>/Rab8<sup>+</sup> tubules are distinct transport intermediates responsible for the biosynthetic delivery of apical membrane proteins in IECs.

To investigate how loss of V-ATPase activity impairs biosynthetic transport of apical, but not basolateral, membrane proteins, we followed p75-GFP transit through apical carriers after a 1-h TGN release during V-ATPase inhibition. As before, control larvae treated with DMSO showed enrichment of p75-GFP at the apical membrane after a 1-h TGN release, with a small population remaining in biosynthetic Rab8<sup>+</sup>/Rab11<sup>+</sup> carriers ([Fig. 9 A](#), arrows; and [Fig. S5, A and B](#), arrows). In contrast, V-ATPase inhibition with bafilomycin acutely blocked p75-GFP delivery through apical carriers ([Fig. 9 A](#), arrowheads; and [Fig. S5, A and B](#), arrowheads). Strikingly, mRFP-Rab8a began condensing into vacuoles within just 1 h of V-ATPase inhibition ([Fig. 9 A](#), asterisks), progressively accumulating there while becoming depleted from Rab11<sup>+</sup> carriers over time ([Fig. S5 C](#)). p75-GFP was largely absent from Rab8 vacuoles at the 1-h time point ([Fig. 9 B](#)) and instead was found surrounding vacuoles in small clusters ([Fig. 9 A](#), bottom, arrowheads and adjacent

asterisks). The relatively rapid (<1 h) collapse of Rab8 to vacuoles was surprising because p75-GFP accumulates in vacuoles with slower kinetics after ~4 h of V-ATPase inhibition ([Fig. 5 E](#), asterisks), suggesting that Rab8 vacuoles fuse with apical carriers over time. Closer inspection revealed that, despite Rab8 mislocalization, p75-GFP was still present along tubules ([Fig. 9, A, C, and D](#), arrowheads) that were closely interspersed with vacuoles ([Fig. 9, C and D](#), asterisks) after a 1-h TGN release with V-ATPase inhibition. At later time points (8-h TGN release plus V-ATPase inhibition), p75-GFP strongly overlapped with mRFP-Rab8a vacuoles ( $R = 0.713 \pm 0.13$ ; six cells, two animals; [Fig. 9, E and F](#)), further indicating that Rab8 vacuoles fuse with apical biosynthetic carriers upon loss of V-ATPase function. Interestingly, although Rab8<sup>+</sup> vacuoles seemed to fuse with post-Golgi tubules during V-ATPase inhibition, Rab11 localization was unaffected by bafilomycin treatment ([Fig. 9 G](#)), suggesting unique requirements for V-ATPase function in post-Golgi Rab8<sup>+</sup> tubules. By contrast, basolateral MICA-GFP, which did not significantly accumulate at vacuoles in our assays ([Fig. S5, D and E](#)), was absent from mRFP-Rab8a tubules during biosynthetic transport in WT larvae ([Fig. S5 F](#)). These data indicate that mRFP-Rab8a tubules are specialized in apical membrane protein trafficking in the intestine.

To determine how V-ATPase function impacts the Rab8<sup>+</sup> compartment, we performed live imaging of mRFP-Rab8a in the intestine after 1 h of bafilomycin treatment ([Fig. 9 H](#)). Control larvae treated with DMSO showed rapid, dynamic movement of mRFP-Rab8a along tubules ([Fig. 9, I and J](#), arrowheads; [Video 2](#), and [Video 3](#)). In contrast, during V-ATPase inhibition, mRFP-Rab8a accumulated in vacuolar structures largely devoid of tubulation ([Fig. 9, I and J](#), arrows; and [Video 2, Video 3](#), and [Video 4](#)). In cases where vacuoles did project outward tubules, they appeared to contact other carriers and vacuoles before coalescing ([Fig. S5 G](#), arrowheads; and [Video 5](#)), supporting the notion that aberrant Rab8<sup>+</sup> vacuoles recruit and fuse with apical biosynthetic carriers. Our live imaging experiments also showed that Rab8<sup>+</sup> tubules rapidly collapsed during V-ATPase inhibition, with multiple Rab8<sup>+</sup> tubules and puncta giving rise to an enlarged vacuole within 25 min ([Fig. S5 G](#), arrowheads; and [Video 5](#)). These data indicate that luminal acidification of apical carriers is required for proper biogenesis and dynamics of Rab8<sup>+</sup> compartments, thereby regulating apical but not basolateral membrane protein trafficking.

## Discussion

In this work, we performed a visual forward genetic screen to identify regulators of apical membrane biogenesis in the

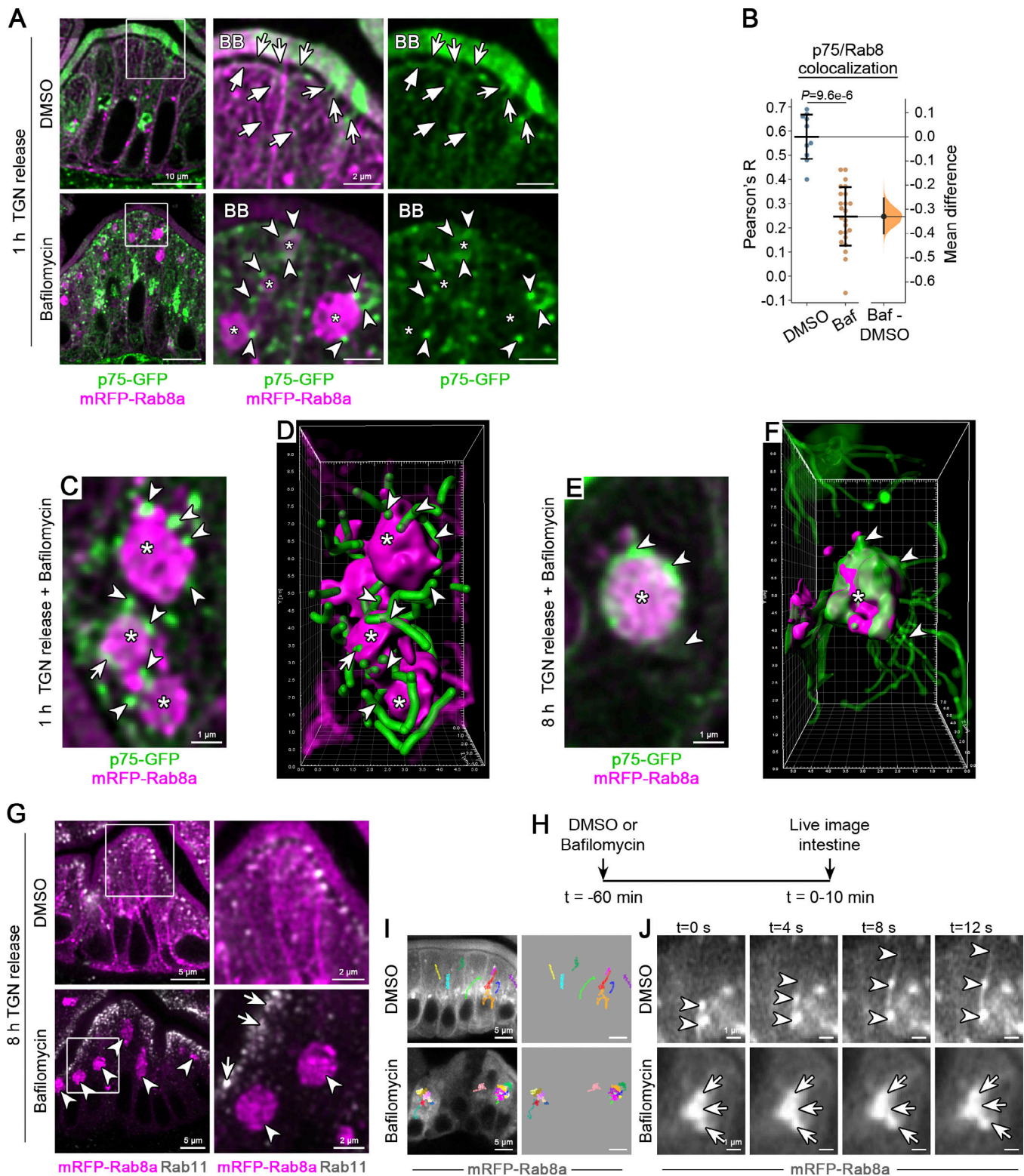


Figure 9. **Acute loss of V-ATPase function rapidly collapses apical Rab8 tubules into vacuoles that fuse with apical carriers.** (A) p75-GFP was imaged in mRFP-Rab8a expressing larvae after a 1-h TGN release in the presence of 750 nM bafilomycin or DMSO as a control. In controls, p75-GFP overlaps with mRFP-Rab8a in post-Golgi tubules (flat arrows) and apical tubules (concave arrows). Upon loss of V-ATPase function, mRFP-Rab8a condenses into vacuoles (asterisks) surrounded by p75-GFP (arrowheads). Scale bars are 10  $\mu$ m and 2  $\mu$ m in magnified insets. (B) Colocalization analysis of p75-GFP and mRFP-Rab8a from ROIs of the apical cytoplasm from  $\sim$ 5  $\mu$ m z-series shown as a Gardner-Altman plot of Pearson's coefficient (R). Left, mean  $\pm$  SD is plotted. Right, mean difference (Baf-DMSO) plotted on a floating axis as a bootstrap sampling distribution with the mean difference depicted as a dot; the 95% confidence interval is indicated by the ends of the vertical error bar.  $n \geq 10$  ROIs from at least two animals.  $P = 9.6e-6$ , Mann-Whitney test. (C) Optical section taken from a 5- $\mu$ m z-series of a group of mRFP-Rab8a vacuoles (asterisks) and p75-GFP tubules (arrowheads), some of which appear to be fusing with vacuoles (arrow), after a 1-h

TGN release in the presence of 750 nM bafilomycin. Scale bar is 1  $\mu\text{m}$ . **(D)** 3D reconstruction of the z-series from C. Highlighted structures correspond approximately to those in E. **(E)** Optical section taken from a 7- $\mu\text{m}$  z-series of an mRFP-Rab8a vacuole (asterisk) and p75-GFP (arrowheads) after an 8-h TGN release in the presence of 500 nM bafilomycin. Scale bar is 1  $\mu\text{m}$ . **(F)** 3D reconstruction of the z-series from E. Highlighted structures correspond approximately to those in E. **(G)** mRFP-Rab8a expressing larvae were treated as in E and stained for endogenous Rab11. In bafilomycin-treated larvae, Rab11 (arrows) remains enriched subapically and does not localize to mRFP-Rab8a vacuoles (arrowheads). Scale bars are 5  $\mu\text{m}$  and 2  $\mu\text{m}$  in magnified insets.  $n \geq 10$  larvae. **(H–J)** Loss of V-ATPase activity acutely impairs Rab8 dynamics along tubular carriers. **(H)** Experimental strategy. 5-dpf larvae expressing mRFP-Rab8a were treated with either 1  $\mu\text{M}$  bafilomycin or DMSO for 45 min before live imaging. **(I)** Overlay of dynamic mRFP-Rab8a tracks (multicolored lines) superimposed on still frames from live imaging videos. Scale bars are 5  $\mu\text{m}$ . **(J)** Magnified insets of still frames from videos represented in I. Arrowheads mark Rab8 moving along tubules in controls, and arrows show Rab8 vacuoles deficient in tubulation during bafilomycin treatment. Scale bars are 1  $\mu\text{m}$ . See also [Video 2](#), [Video 3](#), and [Video 4](#).  $n \geq 6$  larvae. Baf, bafilomycin.

zebrafish intestine. We recovered five mutants representing four phenotypic classes that exhibit robust mislocalization of the apical membrane protein p75-GFP. By characterizing one of these novel mutants, *atp6apl<sup>pd1209</sup>*, we have uncovered distinct roles for V-ATPase function in both the initial sorting of apical membrane proteins at the TGN and their later trafficking through Rab8 tubular carriers ([Fig. 10](#)). Mutants of the V-ATPase complex retain apical membrane proteins intracellularly in aberrant vacuoles, which also accumulate lysosomal membrane proteins and cargo internalized from the intestinal lumen. Remarkably, the requirement for V-ATPase function is specific to apical but not basolateral transport. We found this is due to the fact that loss of V-ATPase activity rapidly collapses Rab8 tubules into vacuoles. Over time, Rab8<sup>+</sup> vacuoles fuse with newly made apical biosynthetic carriers, sequestering apical and some lysosomal membrane proteins, while not affecting basolateral cargo. In addition to its role in post-Golgi trafficking, V-ATPase-dependent acidification also regulates

sorting of O-glycosylated, but not N-glycosylated, apical membrane proteins. Altogether, our study reveals that apical membrane proteins rely on luminal acidification for multiple stages of biosynthetic transport in the intestine.

### Post-Golgi trafficking of apical membrane proteins

Prior studies have shown that in *Rab8a* null mutant knockout (KO) mice, apical membrane proteins accumulate in vacuoles that contain lysosomal cargo and, in some cases, also microvilli ([Sato et al., 2007, 2014](#)), clearly establishing a role for Rab8 in apical membrane biogenesis. Detailed studies *in vitro* have also established requirements for Rab8 in late events of apical transport, affecting lumen formation in 3D cultures ([Bryant et al., 2010](#); [Gálvez-Santisteban et al., 2012](#); [Mrozowska and Fukuda, 2016](#)). Using *in vivo* assays, we found that the V-ATPase regulates post-Golgi biosynthetic trafficking through Rab8<sup>+</sup> tubular carriers, starting at the exit of the TGN. However, unlike *Rab8a* KO mice, we did not observe formation of

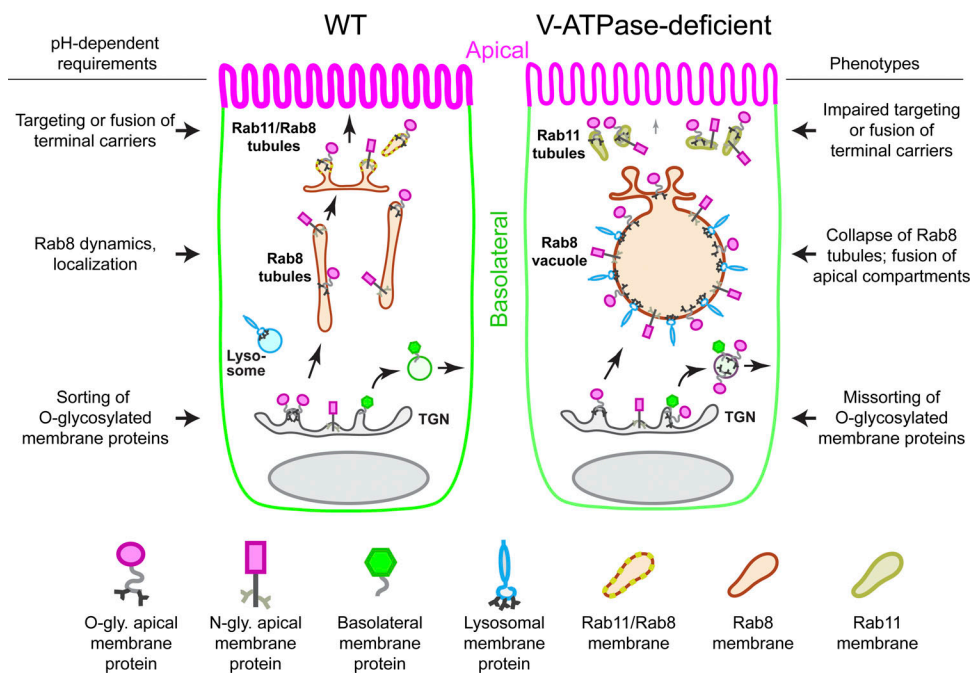


**Figure 10. Model depicting requirements of V-ATPase activity for biosynthetic sorting and trafficking of apical membrane proteins.** V-ATPase activity promotes apical sorting of O-glycosylated membrane proteins in the TGN and subsequent trafficking of both O- and N-glycosylated membrane proteins through distinct Rab8 and Rab11 carriers. In the absence of V-ATPase activity, O-glycosylated membrane proteins become randomly missorted to basolateral and apical trafficking routes. Additionally, apical delivery through Rab11 carriers is acutely blocked, and Rab8 tubular carriers collapse into vacuoles. Over time, aberrant vacuoles fuse with apical compartments and accumulate apical and lysosomal membrane proteins.

microvillus (MV) inclusions in V-ATPase mutants. MV inclusions derive primarily from defective recycling following plasma membrane internalization, but can also form de novo when soluble apical proteins accumulate at apical endosomes (Mosa et al., 2018; Schneeberger et al., 2018; Bidaud-Meynard et al., 2019). *Rab8a* KO mice not only exhibit MV inclusions, but also accumulation of apical membrane proteins within vacuoles that are separate from MV inclusions (Sato et al., 2007). Our study suggests that vacuolar accumulations largely represent biosynthetic transport defects, as we show in zebrafish V-ATPase mutants, while MV inclusions may form separately due to additional defects in internalization and recycling. Because the V-ATPase is primarily required for biosynthetic transport and does not affect soluble apical proteins like villin (Fig. S3 B), its loss may not substantially impact Rab8's role in apical membrane internalization. Interestingly, a recent study in *C. elegans* found that knockdown of V-ATPase  $V_0$  membrane subunits led to MV inclusions while not affecting trafficking of apical membrane proteins. Moreover, its role was unrelated to acidification because most apical polarity defects were not recapitulated either by pH neutralization or by loss of  $V_1$  subunits (Bidaud-Meynard et al., 2019). Together, these studies suggest that, although V-ATPase has a conserved role in intestinal homeostasis, it may also exhibit specialized functions unique to invertebrates.

#### pH-dependent sorting of apical membrane proteins

Our characterization of V-ATPase function in membrane protein transport uncovered a role for luminal acidification in apical sorting of specific classes of membrane proteins. We found that acute neutralization of luminal pH during biosynthetic transport resulted in basolateral missorting of O-glycosylated p75-GFP but not N-glycosylated CD36-GFP or NaPi-2b-intGFP. Similarly, genetic perturbation of the V-ATPase led to basolateral missorting of O-glycosylated membrane proteins p75-GFP, aminopeptidase, and mucins, but not N-glycosylated NaPi-2b-intGFP, nor any basolateral membrane proteins at steady-state. These data argue that sorting deficits did not derive from global loss of epithelial polarity and suggest instead a direct role for luminal acidification in apical sorting.

How could luminal acidification impact apical sorting? One possibility is that an acidic luminal environment promotes clustering of O-glycosylated membrane proteins. Luminal O-glycans are a common sorting signal for apical membrane proteins (Weisz and Rodriguez-Boulan, 2009), and they function by promoting the formation of high molecular weight clusters in the TGN (Cao et al., 2012). Clustering, which is mediated by carbohydrate-carbohydrate interactions (CCIs) and protein-lipid interactions, relies on weak electrostatic interactions such as hydrogen bonding and van der Waals forces (Bucior et al., 2004; Hakomori, 2004). As such, CCIs are sensitive to factors that contribute additional coordinating forces, including divalent cations such as  $Ca^{2+}$ , that alleviate repulsive interactions of negatively charged glycan chains (Haseley et al., 2001; Bucior et al., 2004). We speculate that V-ATPase-dependent acidification promotes neutralization of charges in O-glycans of apical membrane proteins and possibly also in glycolipids, thereby facilitating glycan clustering at the TGN.

In addition to CCIs, pH may also influence binding of lectins such as galectin-3 (Delacour et al., 2006). At steady-state, *Lgals3* (galectin-3) KO mice show missorting of p75 (Delacour et al., 2008), and knockdown of galectin-3 impairs p75 clustering in vitro (Delacour et al., 2007). However, galectin-3 was shown to associate with high molecular weight p75 clusters after TGN release (Delacour et al., 2007), suggesting it functions in a post-Golgi compartment rather than at the TGN, where p75 clustering is initiated (Youker et al., 2013). Moreover, zebrafish V-ATPase mutants exhibit missorting phenotypes distinct from *Lgals3* KO mice. For example, V-ATPase mutants missort aminopeptidase (Fig. 3 C and Fig. S1 H, arrowheads), but *Lgals3* KO mice do not (Delacour et al., 2008). Together, these data are consistent with a role for V-ATPase in sorting that is part of a biophysical process that may later be stabilized and enhanced by other factors such as galectin-3.

#### Sorting and trafficking of lysosomal membrane proteins

We found that apical and lysosomal membrane proteins accumulate together in vacuoles in V-ATPase mutants, suggesting that they share common Rab8-dependent transport intermediates that are segregated from basolateral membrane proteins. Extensive work in mammalian cells has shown that sorting of lysosomal membrane proteins occurs either directly during intracellular transport or indirectly following plasma membrane delivery (Braulke and Bonifacino, 2009). Interestingly, it was recently shown that in HeLa cells, LAMP1 exits the TGN in tubular carriers co-occupied by plasma membrane proteins (Chen et al., 2017), suggesting that some lysosomal membrane proteins undergo progressive sorting. Our data support this model and suggest that in polarized epithelial cells, LAMPs are first segregated to the apical transport pathway. Notably, lysosomal membrane proteins are heavily glycosylated within their luminal domains, much like apical membrane proteins, and these moieties could also serve as additional sorting signals as they do for apical membrane proteins. It will be interesting to determine whether glycan-based sorting acts cooperatively with lysosomal sorting motifs such as dileucine-based and tyrosine-based sequences in polarized epithelial cells.

In conclusion, our study has uncovered distinct roles for V-ATPase-dependent luminal acidification in both initial sorting and later trafficking of apical membrane proteins in vivo. Our study helps to clarify how polarized transport in epithelial cells is regulated and offers future avenues for further dissecting biophysical mechanisms underlying apical sorting. This work could be aided by the characterization of additional mutations exhibiting distinct sorting and trafficking phenotypes from our forward genetic screen. Significantly, our screen did not achieve saturation, suggesting that our forward genetics approach could be expanded and adapted to analyze transport of other cargoes.

## Materials and methods

### Zebrafish maintenance

Zebrafish (*Danio rerio*) were used in accordance with Duke University Institutional Animal Care and Use Committee guidelines. Zebrafish stocks were maintained and bred as



previously described (Westerfield, 2007). Genotypes were determined by fin clipping or phenotypic analysis. Male and female breeders from 3–18 mo of age were used to generate fish for all experiments. 5–6-dpf zebrafish larvae from the Ekkwill or AB/TL background were used in this study. Strains generated for this study: *aa24.2/atp6ap1b*<sup>pd1209</sup>, *bb20.14*<sup>pd1216</sup>, *bx67.16*<sup>pd1217</sup>, *bx38.22*<sup>pd1218</sup>, *cx20.16*<sup>pd1215</sup>, *Tg(ifabp2:p75-GFP)*<sup>pd1208</sup>, *Tg(hsp70l:slc34a2a-intGFP;cmlc2:GFP)*<sup>pd1193</sup> [Napi-2b-intGFP], *Tg(hsp70l:MICA-GFP;cmlc2:GFP)*<sup>pd1183</sup>, *Tg(hsp70l:aqp3-GFP;cmlc2:GFP)*<sup>pd1192</sup>, *Tg(hsp70l:p75-GFP)*<sup>pd1180</sup>, *Tg(ifabp2:B4GALT1-tagRFPt)*<sup>pd1193</sup>, *Tg(hsp70l:cd36-GFP;cmlc2:GFP)*<sup>pd1197</sup>, *Tg(quas:mRFP-rab8a;cmlc2:GFP)*<sup>pd1213</sup>, *Tg(quas:atp6ap1b-intGFP;cryaa:mCherry)*<sup>pd1178</sup>, *Tg(quas:atp6ap1b-intHA-BioID2;cryaa:mCherry)*<sup>pd1176</sup>, and *Tg(quas:B4GALT1-se-pHluorin-tagRFPt;cmlc2:GFP)*<sup>pd1212</sup>. Previously published strains used for this study include: *atp6ap1b*<sup>hi1127g</sup> (Nuckels et al., 2009), *atp6v0ca*<sup>hi11207</sup> (Nuckels et al., 2009), *atp6v1e1*<sup>hi577a</sup> (Nuckels et al., 2009), *atp6v1f*<sup>hi1988</sup> (Nuckels et al., 2009), *atp6ap2*<sup>hi3681</sup> (Amsterdam et al., 2004), *atp6v0d1*<sup>hi2188b</sup> (Nuckels et al., 2009), *atp6v1h*<sup>hi923</sup> (Nuckels et al., 2009), *atp6v1aa*<sup>sa20406</sup> (Busch-Nentwich et al., 2013), *TgBAC(lamp2-RFP)*<sup>pd1044</sup> (Rodríguez-Fraticelli et al., 2015), *cdh1-mLanYFP*<sup>xt17</sup> (Cronan et al., 2018; Cronan and Tobin, 2019), *Tg(cldn15la:qf2;cmlc2:GFP)*<sup>pd1142</sup> (Park et al., 2019), and *TgBAC(cd36-RFP)*<sup>pd1213</sup> (Ye et al., 2019).

### Mutagenesis

Mutagenesis was performed as previously described (Ryan et al., 2013). Adult AB/TL males were exposed to 3 mM ENU in system water for 1 h at 22°C. ENU treatment was repeated six times within a period of 12 wk. Mutagenized males were crossed to AB/TL females to generate F1 families. F1 fish were crossed to the *Tg(ifabp2:p75-GFP)*<sup>pd1208</sup> line to generate F2 families. F2 fish were incrossed, and their F3 progeny were screened at 5 dpf for recessive mutant phenotypes.

### Transgenesis

Constructs used to generate transgenic lines were made using the Tol2kit approach (Kwan et al., 2007) with multisite Gateway cloning (ThermoFisher Scientific). p5E:quas was provided by Marnie Halpern (Carnegie Institution for Science, Baltimore, MD; Subedi et al., 2014). pGEM-rab8a was provided by Rob Parton (University of Queensland, Brisbane, Australia; Hall et al., 2017). pShuttle:B4GALT1-tagRFPt was provided by Norma Andrews (University of Maryland, College Park, MD; Flannery et al., 2010). A plasmid encoding super-ecliptic pHluorin was provided by Cedric Asensio (University of Denver, Denver, CO; Hummer et al., 2017). *slc34a2a* was cloned from zebrafish cDNA into pCS2<sup>+</sup> using the primers 5'-cctctcgagCAG AAGGGCAGAAGCAACTT-3' and 5'-ccttctagaTGCATACTGTCA ACTCTGGGTAC3'. A silent mutation was introduced to remove an endogenous SacI site, and then a NheI/SacI cloning site was introduced between the nucleotides encoding amino acids 50–51 using Q5 site-directed mutagenesis (New England BioLabs). The insertion site was chosen based on a previous study of renal-type NaPi-cotransporter (Lambert et al., 1999). Subsequently, EGFP was cloned into the site, and the fusion was subcloned to a pME Gateway cloning vector (ThermoFisher Scientific). *atp6ap1b* was cloned from zebrafish cDNA to pCS2<sup>+</sup> using the

primers 5'-cctctcgagATGACGGAAGTAGGAATGCG-3' and 5'-ctt tctagaTCACTCACTCAGAGGCACTG-3', and then a NheI/SacI cloning site was introduced between the nucleotides encoding amino acids 241–242 using Q5 site-directed mutagenesis (New England BioLabs). The insertion site was chosen based on previous studies of Ac45 (Louagie et al., 2008; Jansen et al., 2012). EGFP or HA-BioID2 was then cloned to the site, and the fusions were subcloned to pME Gateway cloning vectors (ThermoFisher Scientific). For all other constructs containing N-terminal or C-terminal tags, standard molecular biology approaches were used. To generate stable transgenic lines, one-cell stage embryos were coinjected with Tol2 constructs and transposase cRNA. At 2–3 mpf, the injected fish were outcrossed and their F1 embryos were screened for fluorescence and raised. Individual F1 founders were then outcrossed to obtain stable transgenic lines. All transgenic experiments were performed on larvae of the F2 or greater generations.

### Sectioning, immunofluorescence, and histology

5-dpf larvae were fixed in 4% PFA in PBS (pH 7.5) for 2 h at room temperature or overnight at 4°C, rinsed in PBS, and then embedded in 5% low melting point agarose. 200- $\mu$ m sections were collected using a Leica VT1000S vibratome and stained as previously described (Marjoram et al., 2015). Fluorescently tagged proteins encoded by transgenes were imaged directly unless indicated otherwise. Processing for STED imaging was performed identically, but GFP and RFP were immunostained. Primary antibodies used for confocal imaging were anti-4e8 (Abcam, ab73643), anti-Na<sup>+</sup>K<sup>+</sup>ATPase (DSHB, a5), anti-Rab11, D4F5 clone (Cell Signaling Technology, 5589), and anti-HA (Roche, 11 867 423 001). Goat AlexaFluor-conjugated secondary antibodies (ThermoFisher Scientific) were used for confocal imaging. Antibodies used for STED imaging were anti-GFP (Aves, GFP-1020), FluoTag-Q anti-RFP-AberriorStar-580 conjugate nanobody (Synaptic Systems, N0401-Ab580-S), FluoTag-X2 ATTO 647N-labeled Chicken IgY nanobody (Synaptic Systems, N0702-At647N-S), anti-Rab11, D4F5 clone (Cell Signaling Technology 5589), and goat anti-rabbit IgG AlexaFluor-594 (ThermoFisher Scientific, A-11037). For detection of mucins, 5-dpf larvae were fixed as before but then embedded in JB4-plus plastic resin. 2- $\mu$ m sections were collected using a Reichert-Jung UltraCut microtome equipped with a glass knife as previously described (Levic et al., 2015), stained with periodic acid-Schiff (PAS) and hematoxylin, and mounted in Cytoseal XYL.

### Microscopy, image processing, and image analysis

Whole-mount live confocal imaging was performed on an inverted Olympus Fluoview FV3000 microscope equipped with a 30 $\times$  1.05 NA silicone oil objective. Whole-mount live time-lapse confocal imaging was performed on a Zeiss 880 Airyscan Fast Inverted microscope with a 40 $\times$  1.2 NA water immersion objective. Confocal imaging of tissue sections was performed with either an Olympus Fluoview FV3000 with a 60 $\times$  1.4 NA oil objective or a Leica SP8 with a 100 $\times$  1.4 NA oil objective. Gated STED imaging was performed on a Leica SP8 with a 100 $\times$  1.4 NA oil objective using a pulsed 775-nm laser depletion line for AberriorStar-580, AlexaFluor-594, and ATTO-647N. Confocal

imaging of PAS-stained plastic sections was performed using a Leica SP8 with a 580-nm excitation laser, and emission spectra were collected at a 620–780-nm wavelength. Confocal and STED z-stacks acquired on the Leica SP8 were deconvolved using Huygens Professional linked to LAS X software, as recommended by the manufacturer. Postprocessing of images was performed in ImageJ (National Institutes of Health)/Fiji and Adobe Photoshop. Confocal micrographs were linearly adjusted evenly for brightness and contrast on individual channels and were pseudocolored. Time-lapse videos were corrected for sample drift using the ImageJ (National Institutes of Health) plugin StackReg (Thévenaz et al., 1998), and they were corrected for signal loss from photobleaching using the ImageJ tool Enhance Contrast (National Institutes of Health). Particle tracking was performed in ImageJ (National Institutes of Health) using the plugin MTrackJ (Meijering et al., 2012). 3D rendering of confocal z-stacks was performed in Imaris 9.0 (Bitplane) using the surfaces and filaments tools. Colocalization analysis was performed using ImageJ with the plugin Coloc 2, and R values were plotted and analyzed in GraphPad Prism or using DABEST (data analysis with bootstrap-coupled estimation; Ho et al., 2019). Line scans were collected in ImageJ, plotted in Microsoft Excel, and edited in Photoshop (Adobe). For depictions of colocalized pixels, channels were thresholded, and the resulting double-positive pixels were plotted using the ImageJ plugin Colocalization. For analysis of trafficking phenotypes in Fig. 7, the apical membrane was thresholded using phalloidin signal to automatically select the apical membrane. Mean pixel intensity ratios for the apical membrane and remaining cell area were plotted and analyzed in GraphPad Prism.

### Gavage

5-dpf larvae were gavaged as previously described (Cocchiari and Rawls, 2013). Larvae were gavaged with 4 nl of a mixture containing 10  $\mu$ M LysoTracker Red (ThermoFisher Scientific), 500  $\mu$ M FM4-64 (ThermoFisher Scientific), or 1.25 mg/ml Transferrin-AlexaFluor-568 (ThermoFisher Scientific) in PBS plus 0.05% phenol red. For gavage pulse-chase analysis, larvae were gavaged with one of the solutions above, transferred back to egg water to recover for 90 min, and then gavaged with excess PBS (1–2 pulses of 5–10 nl each), which displaces contents of the intestinal lumen through the cloaca. Flushing of the intestinal lumen was visually assessed by confirming thorough displacement of phenol red from the gut. The chase period proceeded for 90 min, and then larvae were processed for sectioning and confocal imaging. In other experiments, larvae were gavaged with inhibitors, ionophores, or control vehicles dissolved in egg water (pH 7.5) plus 0.05% phenol red. Concentrations and durations used are indicated in the figure legends.

### Analysis of TGN pH

For generation of a calibration curve, 5-dpf larvae stably expressing a TGN-localized luminal pH sensor (*Tg(quas:B4GALT1-se-pHluorin-tagRFPt;cmlc2:GFP)<sup>pd1212</sup>; Tg(cldn15la:qf2;cmlc2:GFP)<sup>pd1142</sup>*) were fixed and sectioned as described above. 200- $\mu$ m-thick sections of the mid-intestine were permeabilized overnight in PBS-0.5% Triton-X100 and then for 10 min in PBS-1% Triton-

X100, and finally equilibrated in pH-calibrated phosphate-citrate buffers (pH 4–8.6) in 20% glycerol for 4 h. Confocal image acquisition settings were assigned at pH 7.5 to allow for high dynamic range with no pixel saturation. Next, intestinal sections for the entire pH range were imaged using these defined confocal imaging parameters. Raw 16-bit confocal images were analyzed in ImageJ/Fiji, and GFP/RFP intensity ratios were plotted in GraphPad Prism. A sigmoidal model was used for curve fitting. For analysis of TGN pH in live animals, whole mount imaging of the intestine was performed in vivo using identical hardware and acquisition settings as assigned for standard curve analysis. Raw 16-bit confocal images were analyzed as before, but for every image, a background subtraction step was performed to correct for autofluorescence that occurs with in vivo imaging. Randomly selected regions of interest (ROIs) were identified using the RFP channel, and GFP/RFP intensity measurements of the TGN were collected. GFP/RFP intensity ratios were used to extrapolate pH values from the calibration curve, and data were analyzed in GraphPad Prism using one-way ANOVA.

### Exome sequencing and mapping

DNA extraction, exome capture, sequencing, and positional cloning were performed exactly as described previously (Ryan et al., 2013). Data were analyzed using SNPtrack (OmicX; Leshchiner et al., 2012). The number of animals analyzed and recombinants observed from positional mapping are presented in Fig. 2 B.

### In vivo low temperature block

5-dpf larvae transgenic for *hsp70l*-inducible EGFP-tagged membrane proteins were transferred to 50-ml conical tubes in 45 ml of egg water ( $n \leq 80$  larvae per tube). Tubes were floated in a 42°C water bath for 30 min to induce transgene expression. Next, for TGN block, tubes were transferred to a 14°C water bath (made using an ice water bath in a thick-walled Styrofoam box) and allowed to float for 2–4 h. For TGN release, larvae were transferred into a 12-well plate at a density of  $\leq 5$  fish/ml, the media were replaced with prewarmed media containing inhibitors, ionophores, or control vehicles, and the plates were incubated at 28°C for the time intervals indicated. Treatment concentrations and durations are described in the figure legends. For kinetic analysis of TGN-to-apical membrane transport, intestinal sections were imaged with confocal microscopy, ROIs of the BB and the remaining cell area were taken for individual cells, and ratios of apical membrane intensity over cytoplasm intensity were plotted and fitted with a one-phase exponential association model in GraphPad Prism. For live imaging of TGN release, larvae were processed for a TGN block as described above and then immediately mounted in 1.3% low melting point agarose in glass-bottom dishes, which were then transferred to a prewarmed 28°C incubation chamber in a Zeiss 880 inverted confocal microscope. EGFP was used as a tag for all TGN release experiments in this study.

### IP and mass spectroscopy

For p75-GFP IP,  $n = 20$  6-dpf larvae were homogenized in T-PER extraction buffer (ThermoFisher Scientific) supplemented with

deoxycholate, EDTA, and protease inhibitors (Sigma, 539134; plus 1  $\mu$ M PMSF), clarified by centrifugation, and incubated with GFP-Trap agarose beads (Chromotek). Eluted proteins were run on an SDS-PAGE gel, and Western blot analysis was performed using anti-GFP (VAPR, 1C9A5) and anti-mouse-HRP antibodies with chemiluminescence in a ChemiDoc Imaging System (Bio-Rad). For 4e8 IP,  $n = 1,000$  5-dpf larvae were homogenized in T-PER extraction buffer (ThermoFisher Scientific) supplemented with deoxycholate, EDTA, and protease inhibitors (Sigma, 539134; plus 1  $\mu$ M PMSF), clarified by centrifugation, and incubated with 10  $\mu$ g of 4e8 antibody (Abcam, ab73643) or 10  $\mu$ g of 2h9 antibody (a different mouse monoclonal antibody used as a control) overnight at 4°C while rotating. Lysate-antibody mixtures were then incubated with Protein G agarose beads (ThermoFisher Scientific, 20398) and washed according to the manufacturer's recommendations. Proteins were eluted with Laemmli buffer and run on an SDS-PAGE gel (BioRad, 4561094). Gels were stained with GelCode Blue Coomassie reagent (ThermoFisher Scientific), and relevant bands were excised and subjected to in-gel trypsin digestion. Extracted peptides were lyophilized and resuspended in 12  $\mu$ l of 1% trifluoroacetic acid/2% acetonitrile. Each sample was subjected to chromatographic separation on a NanoAcquity UPLC equipped with a 1.7- $\mu$ m BEH130 C18 75- $\mu$ m ID  $\times$ 250-mm reversed-phase column. The mobile phase consisted of 0.1% formic acid in water (A) and 0.1% formic acid in acetonitrile (B). Following a 4- $\mu$ l injection, peptides were trapped for 3 min on a 5- $\mu$ m Symmetry C18 180  $\mu$ m ID  $\times$  20 mm column at 5  $\mu$ l/min in 99.9% A. The analytical column was then switched in-line and a linear elution gradient of 5%–30% B was performed over 90 min at 400 nl/min. The analytical column was connected to a fused silica PicoTip emitter (New Objective) with a 10- $\mu$ m tip orifice and coupled to a QExactive HF mass spectrometer (ThermoFisher Scientific) through an electrospray interface operating in a data-dependent mode of acquisition. The instrument was set to acquire a precursor mass spectrometry (MS) scan at  $m/z$  375–1600 with a target automatic gain control value of 3e6 ions, followed by 12 MS/MS scans at an rpm of 15,000 (at  $m/z$  200) at a target automatic gain control value of 5e4 ions and 45 ms. A 20-s dynamic exclusion was employed for previously fragmented precursor ions. Raw liquid chromatography MS/MS data files were processed in Proteome Discoverer (ThermoFisher Scientific) and then submitted to independent Mascot searches (Matrix Science) against a TrEMBL database containing both forward and reverse entries of each protein (59,273 forward entries). Search tolerances were 5 ppm for precursor ions and 0.02 D for product ions using trypsin specificity with up to two missed cleavages. All searched spectra were imported into Scaffold (v4.4; Proteome Software), and scoring thresholds were set to achieve a peptide false discovery rate of 1% using the PeptideProphet algorithm.

#### RT-PCR

20 5-dpf *aa24.2* mutant larvae or WT siblings were homogenized in TRIzol Reagent (Ambion). Total RNA was isolated by phase separation and isopropanol precipitation, treated with DNase I (New England BioLabs), and then purified by acid phenol-chloroform extraction and isopropanol-ammonium acetate

precipitation. Poly-dT-primed first-strand cDNA synthesis was performed using SuperScript III reverse transcription (Invitrogen) with 1  $\mu$ g total RNA, and *atp6apl*b was PCR amplified using the primers 5'-TCCAGCAGAATGACGGAAGT-3' and 5'-CCACATTAAGGCTGGATGC-3'.

#### Online supplemental material

**Fig. S1** provides supporting evidence that V-ATPase function is required for sorting and trafficking of apical membrane proteins. **Fig. S2** shows that the zebrafish BB antigen 4e8 monoclonal antibody labels Anpep. **Fig. S3** shows characterization of trafficking phenotypes for apical membrane, membrane-associated, and apically internalized cargo in V-ATPase mutants. **Fig. S4** shows design and use of a novel pH sensor transgenic line to quantify TGN luminal acidification in intestinal epithelial cells. **Fig. S5** provides supporting evidence that V-ATPase activity is required for biosynthetic trafficking of apical membrane proteins. **Video 1** shows p75-GFP exiting the TGN in mRFP-Rab8a tubular carriers during biosynthetic transport. **Video 2**, **Video 3**, and **Video 4** show decreased dynamic movement of mRFP-Rab8a along tubules when V-ATPase activity is inhibited. **Video 5** shows mRFP-Rab8a tubules collapsing within a 25-min period to form a vacuole after inhibition of V-ATPase activity.

#### Acknowledgments

We thank the Duke Zebrafish Core for fish maintenance, Alessandro De Simone for help with quantitative analysis, the Duke Light Microscopy Core Facility for providing access to and training for imaging systems, the Duke University School of Medicine for the use of the Proteomics and Metabolomics Shared Resource, which provided proteomics services, and James Evangelista from Abcam Inc. for help with proteomics. We also thank Jeff Gross (University of Pittsburgh, Pittsburgh, PA), Marnie Halpern, John Rawls (Duke University, Durham, NC), Mark Cronan (Max Planck Institute for Infection Biology, Berlin, Germany), David Tobin (Duke University), Cedric Asensio, Norma Andrews, and Martin Kahms (Institute of Medical Physics and Biophysics Cellular Biophysics, Münster, Germany) for sharing zebrafish lines and other reagents. We thank Brigid Hogan, Terry Lechler, Kaelyn Sumigra, and Vann Bennett for critical reading of the manuscript and Andrew Muir for helpful discussions.

This work was supported by National Institutes of Health grants DP2OD006486 and 1R01-DK113123 (to M.B.). D.S.L. was supported by a Duke Training Grant in Digestive Diseases and Nutrition (T32DK007568-26). L.M. was supported by Duke Multidisciplinary Fellowship in Pediatric Lung Disease (grant 5T32HL098099-02) and National Institutes of Health National Research Service Award F32-DK098885-01A1. M.B. is a Howard Hughes Medical Institute Faculty Scholar.

The authors declare no competing financial interests.

Author contributions: D.S. Levic and M. Bagnat designed the study. D.S. Levic performed all experiments except for those shown in Fig. 1, E–I, Fig. 2, A–D, and Fig. S1 D. M. Bagnat designed and performed the genetic screen with help from J. Bagwell and J. Honeycutt. L. Marjoram and S. Ryan performed

the analysis shown in Fig. 2, A–D and Fig. S1 D. D.S. Levic, M. Bagnat, and S. Ryan generated transgenic lines. D.S. Levic and M. Bagnat wrote and edited the manuscript.

Submitted: 29 August 2019

Revised: 20 December 2019

Accepted: 27 January 2020

## References

- Alfalah, M., R. Jacob, U. Preuss, K.-P. Zimmer, H. Naim, and H.Y. Naim. 1999. O-linked glycans mediate apical sorting of human intestinal sucrase-isomaltase through association with lipid rafts. *Curr. Biol.* 9:593–596. [https://doi.org/10.1016/S0960-9822\(99\)80263-2](https://doi.org/10.1016/S0960-9822(99)80263-2)
- Amsterdam, A., R.M. Nissen, Z. Sun, E.C. Swindell, S. Farrington, and N. Hopkins. 2004. Identification of 315 genes essential for early zebrafish development. *Proc. Natl. Acad. Sci. USA.* 101:12792–12797. <https://doi.org/10.1073/pnas.0403929101>
- Apodaca, G., L.I. Gallo, and D.M. Bryant. 2012. Role of membrane traffic in the generation of epithelial cell asymmetry. *Nat. Cell Biol.* 14:1235–1243. <https://doi.org/10.1038/ncb2635>
- Bagnat, M., and K. Simons. 2002. Lipid rafts in protein sorting and cell polarity in budding yeast *Saccharomyces cerevisiae*. *Biol. Chem.* 383: 1475–1480. <https://doi.org/10.1515/BC.2002.169>
- Bagnat, M., S. Keränen, A. Shevchenko, A. Shevchenko, and K. Simons. 2000. Lipid rafts function in biosynthetic delivery of proteins to the cell surface in yeast. *Proc. Natl. Acad. Sci. USA.* 97:3254–3259. <https://doi.org/10.1073/pnas.97.7.3254>
- Bidaud-Meynard, A., O. Nicolle, M. Heck, Y. Le Cunff, and G. Michaux. 2019. A V0-ATPase-dependent apical trafficking pathway maintains the polarity of the intestinal absorptive membrane. *Development.* 146: dev174508. <https://doi.org/10.1242/dev.174508>
- Braulke, T., and J.S. Bonifacino. 2009. Sorting of lysosomal proteins. *Biochim. Biophys. Acta.* 1793:605–614. <https://doi.org/10.1016/j.bbamcr.2008.10.016>
- Breuzer, L., M. Garcia, M.-H. Delgrossi, and A. Le Bivic. 2002. Role of the membrane-proximal O-glycosylation site in sorting of the human receptor for neurotrophins to the apical membrane of MDCK cells. *Exp. Cell Res.* 273:178–186. <https://doi.org/10.1006/excr.2001.5442>
- Brown, D.A., and J.K. Rose. 1992. Sorting of GPI-anchored proteins to glycolipid-enriched membrane subdomains during transport to the apical cell surface. *Cell.* 68:533–544. [https://doi.org/10.1016/0092-8674\(92\)90189-j](https://doi.org/10.1016/0092-8674(92)90189-j)
- Bryant, D.M., A. Datta, A.E. Rodríguez-Fraticelli, J. Peränen, F. Martín-Belmonte, and K.E. Mostov. 2010. A molecular network for de novo generation of the apical surface and lumen. *Nat. Cell Biol.* 12:1035–1045. <https://doi.org/10.1038/ncb2106>
- Bryant, D.M., J. Roignant, A. Datta, A.W. Overeem, M. Kim, W. Yu, X. Peng, D.J. Eastburn, A.J. Ewald, Z. Werb, and K.E. Mostov. 2014. A molecular switch for the orientation of epithelial cell polarization. *Dev. Cell.* 31: 171–187. <https://doi.org/10.1016/j.devcel.2014.08.027>
- Bucior, I., S. Scheuring, A. Engel, and M.M. Burger. 2004. Carbohydrate-carbohydrate interaction provides adhesion force and specificity for cellular recognition. *J. Cell Biol.* 165:529–537. <https://doi.org/10.1083/jcb.200309005>
- Busch-Nentwich, E., R. Kettleborough, C.M. Dooley, C. Scahill, I. Sealy, R. White, C. Herd, S. Mehroke, N. Wali, S. Carruthers, et al. 2013. Sanger Institute Zebrafish Mutation Project mutant data submission. ZFIN Direct Data Submission. Available at: <http://zfin.org> (accessed January 24, 2018).
- Caceres, P.S., I. Benedicto, G.L. Lehmann, and E.J. Rodriguez-Boulan. 2017. Directional fluid transport across organ-blood barriers: physiology and cell biology. *Cold Spring Harb. Perspect. Biol.* 9:a027847. <https://doi.org/10.1101/cshperspect.a027847>
- Cao, X., M.A. Surma, and K. Simons. 2012. Polarized sorting and trafficking in epithelial cells. *Cell Res.* 22:793–805. <https://doi.org/10.1038/cr.2012.64>
- Casey, J.R., S. Grinstein, and J. Orłowski. 2010. Sensors and regulators of intracellular pH. *Nat. Rev. Mol. Cell Biol.* 11:50–61. <https://doi.org/10.1038/nrm2820>
- Chen, Y., D.C. Gershlick, S.Y. Park, and J.S. Bonifacino. 2017. Segregation in the Golgi complex precedes export of endolysosomal proteins in distinct transport carriers. *J. Cell Biol.* 216:4141–4151. <https://doi.org/10.1083/jcb.201707172>
- Cocchiari, J.L., and J.F. Rawls. 2013. Microgavage of zebrafish larvae. *J. Vis. Exp.* 4434:e4434. <https://doi.org/10.3791/4434>
- Cotter, K., L. Stransky, C. McGuire, and M. Forgac. 2015. Recent insights into the structure, regulation, and function of the V-ATPases. *Trends Biochem. Sci.* 40:611–622. <https://doi.org/10.1016/j.tibs.2015.08.005>
- Cronan, M.R., and D.M. Tobin. 2019. Endogenous tagging at the *cdhl* locus for live visualization of E-cadherin dynamics. *Zebrafish.* 16:324–325. <https://doi.org/10.1089/zeb.2019.1746>
- Cronan, M.R., M.A. Matty, A.F. Rosenberg, L. Blanc, C.J. Pyle, S.T. Espenschied, J.F. Rawls, V. Dartois, and D.M. Tobin. 2018. An explant technique for high-resolution imaging and manipulation of mycobacterial granulomas. *Nat. Methods.* 15:1098–1107. <https://doi.org/10.1038/s41592-018-0215-8>
- Delacour, D., V. Gouyer, J.-P. Zanetta, H. Drobecq, E. Leteurtre, G. Grard, O. Moreau-Hannedouche, E. Maes, A. Pons, S. André, et al. 2005. Galectin-4 and sulfatides in apical membrane trafficking in enterocyte-like cells. *J. Cell Biol.* 169:491–501. <https://doi.org/10.1083/jcb.200407073>
- Delacour, D., C.I. Cramm-Behrens, H. Drobecq, A. Le Bivic, H.Y. Naim, and R. Jacob. 2006. Requirement for galectin-3 in apical protein sorting. *Curr. Biol.* 16:408–414. <https://doi.org/10.1016/j.cub.2005.12.046>
- Delacour, D., C. Greb, A. Koch, E. Salomonsson, H. Leffler, A. Le Bivic, and R. Jacob. 2007. Apical sorting by galectin-3-dependent glycoprotein clustering. *Traffic.* 8:379–388. <https://doi.org/10.1111/j.1600-0854.2007.00539.x>
- Delacour, D., A. Koch, W. Ackermann, I. Eude-Le Parco, H.-P. Elsässer, F. Poirier, and R. Jacob. 2008. Loss of galectin-3 impairs membrane polarization of mouse enterocytes in vivo. *J. Cell Sci.* 121:458–465. <https://doi.org/10.1242/jcs.020800>
- Flannery, A.R., C. Czibener, and N.W. Andrews. 2010. Palmitoylation-dependent association with CD63 targets the Ca<sup>2+</sup> sensor synaptotagmin VII to lysosomes. *J. Cell Biol.* 191:599–613. <https://doi.org/10.1083/jcb.201003021>
- Fölsch, H., H. Ohno, J.S. Bonifacino, and I. Mellman. 1999. A novel clathrin adaptor complex mediates basolateral targeting in polarized epithelial cells. *Cell.* 99:189–198. [https://doi.org/10.1016/S0092-8674\(00\)81650-5](https://doi.org/10.1016/S0092-8674(00)81650-5)
- Gálvez-Santisteban, M., A.E. Rodríguez-Fraticelli, D.M. Bryant, S. Vergarajauregui, T. Yasuda, I. Bañón-Rodríguez, I. Bernascone, A. Datta, N. Spivak, K. Young, et al. 2012. Synaptotagmin-like proteins control the formation of a single apical membrane domain in epithelial cells. *Nat. Cell Biol.* 14:838–849. <https://doi.org/10.1038/ncb2541>
- Gravotta, D., J.M. Carvajal-Gonzalez, R. Mattera, S. Deborde, J.R. Banfelder, J.S. Bonifacino, and E. Rodríguez-Boulan. 2012. The clathrin adaptor AP-1A mediates basolateral polarity. *Dev. Cell.* 22:811–823. <https://doi.org/10.1016/j.devcel.2012.02.004>
- Griffiths, G., and K. Simons. 1986. The trans Golgi network: sorting at the exit site of the Golgi complex. *Science.* 234:438–443. <https://doi.org/10.1126/science.2945253>
- Guo, X., R. Mattera, X. Ren, Y. Chen, C. Retamal, A. González, and J.S. Bonifacino. 2013. The adaptor protein-1 μB subunit expands the repertoire of basolateral sorting signal recognition in epithelial cells. *Dev. Cell.* 27:353–366. <https://doi.org/10.1016/j.devcel.2013.10.006>
- Hakomori, S. 2004. Carbohydrate-to-carbohydrate interaction in basic cell biology: a brief overview. *Arch. Biochem. Biophys.* 426:173–181. <https://doi.org/10.1016/j.abb.2004.02.032>
- Hall, T.E., N. Martel, H.P. Lo, Z. Xiong, and R.G. Parton. 2017. A plasmid library of full-length zebrafish rab proteins for *in vivo* cell biology. *Cell. Logist.* 7:e1301151. <https://doi.org/10.1080/21592799.2017.1301151>
- Haseley, S.R., H.J. Vermeer, J.P. Kamerling, and J.F.G. Vliegthart. 2001. Carbohydrate self-recognition mediates marine sponge cellular adhesion. *Proc. Natl. Acad. Sci. USA.* 98:9419–9424. <https://doi.org/10.1073/pnas.151111298>
- Ho, J., T. Tumkaya, S. Aryal, H. Choi, and A. Claridge-Chang. 2019. Moving beyond P values: data analysis with estimation graphics. *Nat. Methods.* 16:565–566. <https://doi.org/10.1038/s41592-019-0470-3>
- Hummer, B.H., N.F. de Leeuw, C. Burns, L. Chen, M.S. Joens, B. Hosford, J.A.J. Fitzpatrick, and C.S. Asensio. 2017. HID-1 controls formation of large dense core vesicles by influencing cargo sorting and trans-Golgi network acidification. *Mol. Biol. Cell.* 28:3870–3880. <https://doi.org/10.1091/mbc.e17-08-0491>
- Jansen, E.J.R., N.H.M. van Bakel, N.F. Olde Loohuis, T.G.M. Hafmans, T. Arentsen, A.J.M. Coenen, W.J.J.M. Scheenen, and G.J.M. Martens. 2012. Identification of domains within the V-ATPase accessory subunit Ac45 involved in V-ATPase transport and Ca<sup>2+</sup>-dependent exocytosis. *J. Biol. Chem.* 287:27537–27546. <https://doi.org/10.1074/jbc.M12.356105>
- Keller, P., D. Toomre, E. Díaz, J. White, and K. Simons. 2001. Multicolour imaging of post-Golgi sorting and trafficking in live cells. *Nat. Cell Biol.* 3:140–149. <https://doi.org/10.1038/35055042>

- Kim, J.H., C.A. Lingwood, D.B. Williams, W. Furuya, M.F. Manolson, and S. Grinstein. 1996. Dynamic measurement of the pH of the Golgi complex in living cells using retrograde transport of the verotoxin receptor. *J. Cell Biol.* 134:1387–1399. <https://doi.org/10.1083/jcb.134.6.1387>
- Klemm, R.W., C.S. Ejsing, M.A. Surma, H.-J. Kaiser, M.J. Gerl, J.L. Sampaio, Q. de Robillard, C. Ferguson, T.J. Proszynski, A. Shevchenko, and K. Simons. 2009. Segregation of sphingolipids and sterols during formation of secretory vesicles at the trans-Golgi network. *J. Cell Biol.* 185:601–612. <https://doi.org/10.1083/jcb.200901145>
- Knowles, B.C., V.G. Weis, S. Yu, J.T. Roland, J.A. Williams, G.S. Alvarado, L.A. Lapierre, M.D. Shub, N. Gao, and J.R. Goldenring. 2015. Rab11a regulates syntaxin 3 localization and microvillus assembly in enterocytes. *J. Cell Sci.* 128:1617–1626. <https://doi.org/10.1242/jcs.163303>
- Kwan, K.M., E. Fujimoto, C. Grabher, B.D. Mangum, M.E. Hardy, D.S. Campbell, J.M. Parant, H.J. Yost, J.P. Kanki, and C.-B. Chien. 2007. The Tol2kit: a multisite gateway-based construction kit for Tol2 transposon transgenesis constructs. *Dev. Dyn.* 236:3088–3099. <https://doi.org/10.1002/dvdy.21343>
- Lambert, G., M. Traebert, N. Hernando, J. Biber, and H. Murer. 1999. Studies on the topology of the renal type II NaPi-cotransporter. *Pflügers Arch.* 437:972–978. <https://doi.org/10.1007/s004240050869>
- Leshchiner, I., K. Alexa, P. Kelsey, I. Adzhubei, C.A. Austin-Tse, J.D. Cooney, H. Anderson, M.J. King, R.W. Stottmann, M.K. Garnas, et al. 2012. Mutation mapping and identification by whole-genome sequencing. *Genome Res.* 22:1541–1548. <https://doi.org/10.1101/gr.135541.111>
- Levic, D.S., J.R. Minkel, W.-D. Wang, W.M. Rybski, D.B. Melville, and E.W. Knapik. 2015. Animal model of Sar1b deficiency presents lipid absorption deficits similar to Anderson disease. *J. Mol. Med. (Berl.)*. 93:165–176. <https://doi.org/10.1007/s00109-014-1247-x>
- Lingwood, D., and K. Simons. 2010. Lipid rafts as a membrane-organizing principle. *Science*. 327:46–50. <https://doi.org/10.1126/science.1174621>
- Louagie, E., N.A. Taylor, D. Flamez, A.J.M. Roebroek, N.A. Bright, S. Meulemans, R. Quintens, P.L. Herrera, F. Schuit, W.J. Van de Ven, and J.W.M. Creemers. 2008. Role of furin in granular acidification in the endocrine pancreas: identification of the V-ATPase subunit Ac45 as a candidate substrate. *Proc. Natl. Acad. Sci. USA*. 105:12319–12324. <https://doi.org/10.1073/pnas.0800340105>
- Maeda, Y., T. Ide, M. Koike, Y. Uchiyama, and T. Kinoshita. 2008. GPHR is a novel anion channel critical for acidification and functions of the Golgi apparatus. *Nat. Cell Biol.* 10:1135–1145. <https://doi.org/10.1038/ncb1773>
- Marjoram, L., A. Alvers, M.E. Deerhake, J. Bagwell, J. Mankiewicz, J.L. Cocchiari, R.W. Beerman, J. Willer, K.D. Sumigray, N. Katsanis, et al. 2015. Epigenetic control of intestinal barrier function and inflammation in zebrafish. *Proc. Natl. Acad. Sci. USA*. 112:2770–2775. <https://doi.org/10.1073/pnas.1424089112>
- Martin-Belmonte, F., A. Gassama, A. Datta, W. Yu, U. Rescher, V. Gerke, and K. Mostov. 2007. PTEN-mediated apical segregation of phosphoinositides controls epithelial morphogenesis through Cdc42. *Cell*. 128:383–397. <https://doi.org/10.1016/j.cell.2006.11.051>
- Matlin, K.S. 1986. The sorting of proteins to the plasma membrane in epithelial cells. *J. Cell Biol.* 103:2565–2568. <https://doi.org/10.1083/jcb.103.6.2565>
- Matlin, K.S., and K. Simons. 1983. Reduced temperature prevents transfer of a membrane glycoprotein to the cell surface but does not prevent terminal glycosylation. *Cell*. 34:233–243. [https://doi.org/10.1016/0092-8674\(83\)90154-X](https://doi.org/10.1016/0092-8674(83)90154-X)
- Maxson, M.E., and S. Grinstein. 2014. The vacuolar-type H<sup>+</sup>-ATPase at a glance - more than a proton pump. *J. Cell Sci.* 127:4987–4993. <https://doi.org/10.1242/jcs.158550>
- Meijering, E., O. Dzyubachyk, and I. Smal. 2012. Methods for cell and particle tracking. *Methods Enzymol.* 504:183–200. <https://doi.org/10.1016/B978-0-12-391857-4.00009-4>
- Mellman, I., and K. Simons. 1992. The Golgi complex: in vitro veritas? *Cell*. 68:829–840. [https://doi.org/10.1016/0092-8674\(92\)90027-A](https://doi.org/10.1016/0092-8674(92)90027-A)
- Miesenböck, G., D.A. De Angelis, and J.E. Rothman. 1998. Visualizing secretion and synaptic transmission with pH-sensitive green fluorescent proteins. *Nature*. 394:192–195. <https://doi.org/10.1038/28190>
- Mishra, R., M. Grzybek, T. Niki, M. Hirashima, and K. Simons. 2010. Galectin-9 trafficking regulates apical-basal polarity in Madin-Darby canine kidney epithelial cells. *Proc. Natl. Acad. Sci. USA*. 107:17633–17638. <https://doi.org/10.1073/pnas.1012424107>
- Mosa, M.H., O. Nicolle, S. Maschalidi, F.E. Sepulveda, A. Bidaud-Meynard, C. Menche, B.E. Michels, G. Michaux, G. de Saint Basile, and H.F. Farin. 2018. Dynamic formation of microvillus inclusions during enterocyte differentiation in *Munc18-2*-deficient intestinal organoids. *Cell. Mol. Gastroenterol. Hepatol.* 6:477–493.e1. <https://doi.org/10.1016/j.jcmgh.2018.08.001>
- Mrozowska, P.S., and M. Fukuda. 2016. Regulation of podocalyxin trafficking by Rab small GTPases in 2D and 3D epithelial cell cultures. *J. Cell Biol.* 213:355–369. <https://doi.org/10.1083/jcb.201512024>
- Naim, H.Y., G. Joberty, M. Alfalah, and R. Jacob. 1999. Temporal association of the N- and O-linked glycosylation events and their implication in the polarized sorting of intestinal brush border sucrose-isomaltase, aminopeptidase N, and dipeptidyl peptidase IV. *J. Biol. Chem.* 274:17961–17967. <https://doi.org/10.1074/jbc.274.25.17961>
- Nakajo, A., S. Yoshimura, H. Togawa, M. Kunii, T. Iwano, A. Izumi, Y. Noguchi, A. Watanabe, A. Goto, T. Sato, and A. Harada. 2016. EHPIL1 coordinates Rab8 and Bin1 to regulate apical-directed transport in polarized epithelial cells. *J. Cell Biol.* 212:297–306. <https://doi.org/10.1083/jcb.201508086>
- Nuckels, R.J., A. Ng, T. Darland, and J.M. Gross. 2009. The vacuolar-ATPase complex regulates retinoblast proliferation and survival, photoreceptor morphogenesis, and pigmentation in the zebrafish eye. *Invest. Ophthalmol. Vis. Sci.* 50:893–905. <https://doi.org/10.1167/iovs.08-2743>
- Orlowski, J., and S. Grinstein. 2011. Na<sup>+</sup>/H<sup>+</sup> exchangers. *Compr. Physiol.* 1:2083–2100. <https://doi.org/10.1002/cphy.c110020>
- Paladino, S., D. Sarnataro, R. Pillich, S. Tivodar, L. Nitsch, and C. Zurzolo. 2004. Protein oligomerization modulates raft partitioning and apical sorting of GPI-anchored proteins. *J. Cell Biol.* 167:699–709. <https://doi.org/10.1083/jcb.200407094>
- Park, J., D.S. Levic, K.D. Sumigray, J. Bagwell, O. Eroglu, C.L. Block, C. Eroglu, R. Barry, C.R. Lickwar, J.F. Rawls, et al. 2019. Lysosome-rich enterocytes mediate protein absorption in the vertebrate gut. *Dev. Cell*. 51:7–20.e6. <https://doi.org/10.1016/j.devcel.2019.08.001>
- Poëa-Guyon, S., M.R. Ammar, M. Erard, M. Amar, A.W. Moreau, P. Fossier, V. Gleize, N. Vitale, and N. Morel. 2013. The V-ATPase membrane domain is a sensor of granular pH that controls the exocytotic machinery. *J. Cell Biol.* 203:283–298. <https://doi.org/10.1083/jcb.201303104>
- Qasba, P.K., B. Ramakrishnan, and E. Boeggeman. 2008. Structure and function of beta -1,4-galactosyltransferase. *Curr. Drug Targets*. 9:292–309. <https://doi.org/10.2174/138945008783954943>
- Rodriguez-Boulant, E., and I.G. Macara. 2014. Organization and execution of the epithelial polarity programme. *Nat. Rev. Mol. Cell Biol.* 15:225–242. <https://doi.org/10.1038/nrm3775>
- Rodriguez-Fraticelli, A.E., J. Bagwell, M. Bosch-Forteza, G. Boncompain, N. Reglero-Real, M.J. García-León, G. Andrés, M.L. Toribio, M.A. Alonso, J. Millán, et al. 2015. Developmental regulation of apical endocytosis controls epithelial patterning in vertebrate tubular organs. *Nat. Cell Biol.* 17:241–250. <https://doi.org/10.1038/ncb3106>
- Ryan, S., J. Willer, L. Marjoram, J. Bagwell, J. Mankiewicz, I. Leshchiner, W. Goessling, M. Bagnat, and N. Katsanis. 2013. Rapid identification of kidney cyst mutations by whole exome sequencing in zebrafish. *Development*. 140:4445–4451. <https://doi.org/10.1242/dev.101170>
- Sankaranarayanan, S., D. De Angelis, J.E. Rothman, and T.A. Ryan. 2000. The use of pHluorins for optical measurements of presynaptic activity. *Biophys. J.* 79:2199–2208. [https://doi.org/10.1016/S0006-3495\(00\)76468-X](https://doi.org/10.1016/S0006-3495(00)76468-X)
- Sato, T., S. Mushiaki, Y. Kato, K. Sato, M. Sato, N. Takeda, K. Ozono, K. Miki, Y. Kubo, A. Tsuji, et al. 2007. The Rab8 GTPase regulates apical protein localization in intestinal cells. *Nature*. 448:366–369. <https://doi.org/10.1038/nature05929>
- Sato, T., T. Iwano, M. Kunii, S. Matsuda, R. Mizuguchi, Y. Jung, H. Hagiwara, Y. Yoshihara, M. Yuzaki, R. Harada, and A. Harada. 2014. Rab8a and Rab8b are essential for several apical transport pathways but insufficient for ciliogenesis. *J. Cell Sci.* 127:422–431. <https://doi.org/10.1242/jcs.136903>
- Scheiffele, P., J. Peränen, and K. Simons. 1995. N-glycans as apical sorting signals in epithelial cells. *Nature*. 378:96–98. <https://doi.org/10.1038/378096a0>
- Schneeberger, K., S. Roth, E.E.S. Nieuwenhuis, and S. Middendorp. 2018. Intestinal epithelial cell polarity defects in disease: lessons from microvillus inclusion disease. *Dis. Model. Mech.* 11:dmm031088. <https://doi.org/10.1242/dmm.031088>
- Schuck, S., and K. Simons. 2004. Polarized sorting in epithelial cells: raft clustering and the biogenesis of the apical membrane. *J. Cell Sci.* 117:5955–5964. <https://doi.org/10.1242/jcs.01596>
- Shaner, N.C., M.Z. Lin, M.R. McKeown, P.A. Steinbach, K.L. Hazelwood, M.W. Davidson, and R.Y. Tsien. 2008. Improving the photostability of bright monomeric orange and red fluorescent proteins. *Nat. Methods*. 5:545–551. <https://doi.org/10.1038/nmeth.1209>

- Simons, K., and W.L.C. Vaz. 2004. Model systems, lipid rafts, and cell membranes. *Annu. Rev. Biophys. Biomol. Struct.* 33:269–295. <https://doi.org/10.1146/annurev.biophys.32.110601.141803>
- Sobajima, T., S. Yoshimura, T. Iwano, M. Kunii, M. Watanabe, N. Atik, S. Mushiake, E. Morii, Y. Koyama, E. Miyoshi, and A. Harada. 2014. Rab11a is required for apical protein localisation in the intestine. *Biol. Open*. 4: 86–94. <https://doi.org/10.1242/bio.20148532>
- Subedi, A., M. Macurak, S.T. Gee, E. Monge, M.G. Goll, C.J. Potter, M.J. Parsons, and M.E. Halpern. 2014. Adoption of the Q transcriptional regulatory system for zebrafish transgenesis. *Methods*. 66:433–440. <https://doi.org/10.1016/j.ymeth.2013.06.012>
- Suemizu, H., M. Radosavljevic, M. Kimura, S. Sadahiro, S. Yoshimura, S. Bahram, and H. Inoko. 2002. A basolateral sorting motif in the MICA cytoplasmic tail. *Proc. Natl. Acad. Sci. USA*. 99:2971–2976. <https://doi.org/10.1073/pnas.052701099>
- Thévenaz, P., U.E. Ruttimann, and M. Unser. 1998. A pyramid approach to subpixel registration based on intensity. *IEEE Trans. Image Process.* 7: 27–41. <https://doi.org/10.1109/83.650848>
- Wandinger-Ness, A., M.K. Bennett, C. Antony, and K. Simons. 1990. Distinct transport vesicles mediate the delivery of plasma membrane proteins to the apical and basolateral domains of MDCK cells. *J. Cell Biol.* 111: 987–1000. <https://doi.org/10.1083/jcb.111.3.987>
- Weis, V.G., B.C. Knowles, E. Choi, A.E. Goldstein, J.A. Williams, E.H. Manning, J.T. Roland, L.A. Lapierre, and J.R. Goldenring. 2016. Loss of MYO5B in mice recapitulates Microvillus Inclusion Disease and reveals an apical trafficking pathway distinct to neonatal duodenum. *Cell. Mol. Gastroenterol. Hepatol.* 2:131–157. <https://doi.org/10.1016/j.jcmgh.2015.11.009>
- Weisz, O.A., and E. Rodriguez-Boulan. 2009. Apical trafficking in epithelial cells: signals, clusters and motors. *J. Cell Sci.* 122:4253–4266. <https://doi.org/10.1242/jcs.032615>
- Westerfield, M. 2007. *The Zebrafish Book: A Guide for the Laboratory Use of Zebrafish (Danio rerio)*. Fifth Edition. University of Oregon Press, Eugene, OR.
- Wu, M.M., M. Grabe, S. Adams, R.Y. Tsien, H.-P.H. Moore, and T.E. Machen. 2001. Mechanisms of pH regulation in the regulated secretory pathway. *J. Biol. Chem.* 276:33027–33035. <https://doi.org/10.1074/jbc.M103917200>
- Ye, L., O. Mueller, J. Bagwell, M. Bagnat, R.A. Liddle, and J.F. Rawls. 2019. High fat diet induces microbiota-dependent silencing of enteroendocrine cells. *eLife*. 8:e48479. <https://doi.org/10.7554/eLife.48479>
- Yeaman, C., A.H. Le Gall, A.N. Baldwin, L. Monlauzeur, A. Le Bivic, and E. Rodriguez-Boulan. 1997. The O-glycosylated stalk domain is required for apical sorting of neurotrophin receptors in polarized MDCK cells. *J. Cell Biol.* 139:929–940. <https://doi.org/10.1083/jcb.139.4.929>
- Youker, R.T., J.R. Bruns, S.A. Costa, Y. Rbaibi, F. Lanni, O.B. Kashlan, H. Teng, and O.A. Weisz. 2013. Multiple motifs regulate apical sorting of p75 via a mechanism that involves dimerization and higher-order oligomerization. *Mol. Biol. Cell*. 24:1996–2007. <https://doi.org/10.1091/mbc.e13-02-0078>
- Zhang, H., N. Abraham, L.A. Khan, D.H. Hall, J.T. Fleming, and V. Göbel. 2011. Apicobasal domain identities of expanding tubular membranes depend on glycosphingolipid biosynthesis. *Nat. Cell Biol.* 13:1189–1201. <https://doi.org/10.1038/ncb2328>

## Supplemental material

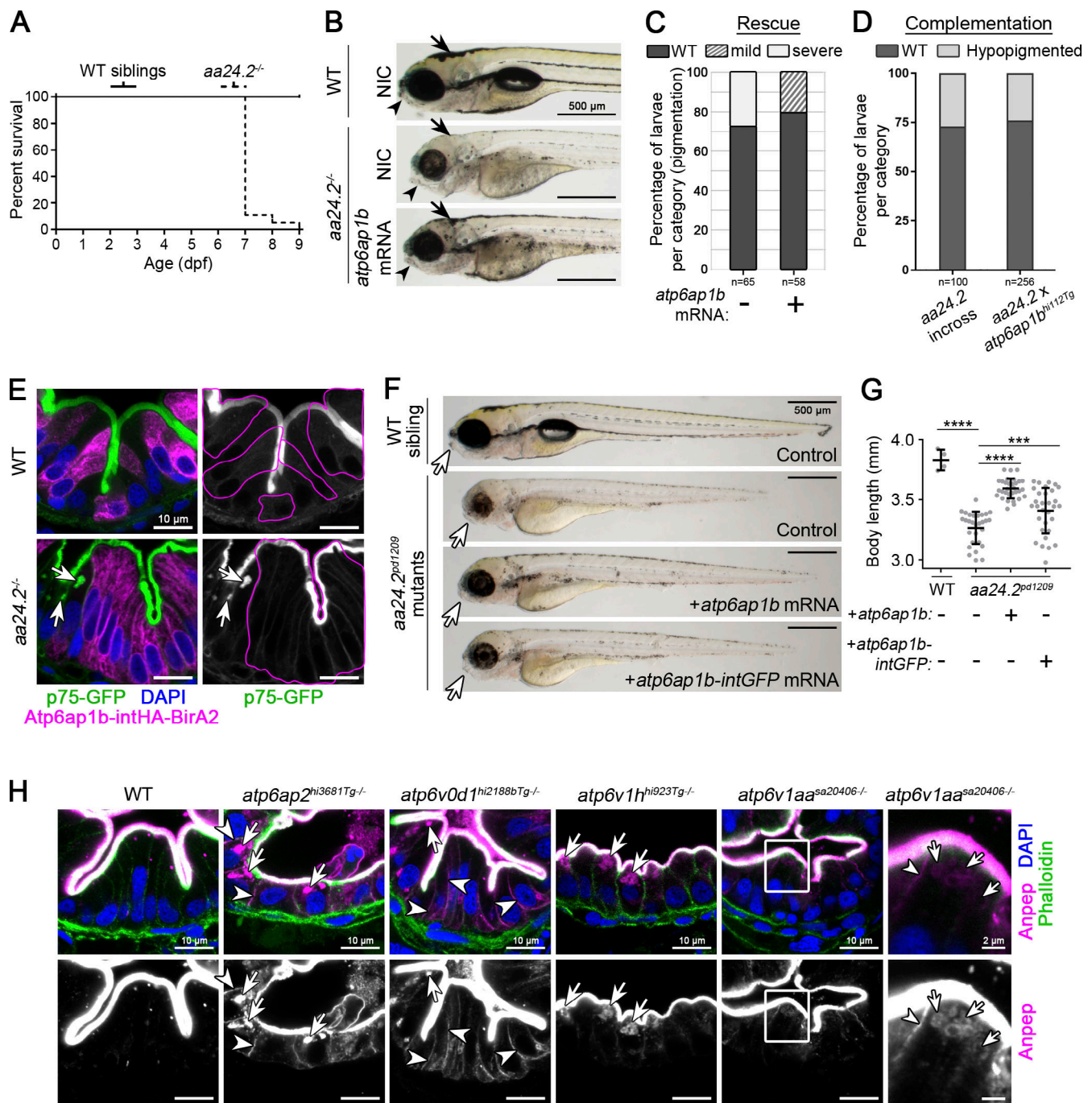


**Figure S1. Loss of *atp6ap1b* is causative of *aa24.2<sup>pd1209</sup>* mutant phenotypes.** (A) Survival curve of *aa24.2<sup>pd1209</sup>* mutants.  $n = 82$  mutants and 109 WT siblings. (B–G) Rescue experiments for *aa24.2<sup>pd1209</sup>* mutants. (B) *aa24.2<sup>pd1209</sup>* heterozygotes were crossed, and one-cell stage embryos were injected with *atp6ap1b* cRNA with a portion of embryos kept as noninjected controls (NIC) and analyzed at 4 dpf for craniofacial dysmorphism (arrowheads) and hypopigmentation (arrows). Scale bar is 500  $\mu\text{m}$ . (C) Quantitation of hypopigmentation. Severe is denoted as the *aa24.2<sup>pd1209</sup>* NIC phenotype shown in A, which is fully penetrant in control mutants. (D) Complementation analysis of the *aa24.2<sup>pd1209</sup>* allele with the *atp6ap1b<sup>hi112Tg</sup>* allele previously described (Nuckels et al., 2009).  $n$  values are shown in C and D. (E) Mosaic expression of HA-tagged Atp6ap1b in enterocytes cell-autonomously rescues p75-GFP localization in *aa24.2<sup>pd1209</sup>* mutants. Magenta lines indicate HA-positive cells and arrows point to intracellular accumulation. Scale bars are 10  $\mu\text{m}$ .  $n > 10$  mutants in two independent experiments. (F and G) *aa24.2<sup>pd1209</sup>* heterozygotes were crossed, and one-cell stage embryos were injected with cRNA encoding untagged or GFP-tagged Atp6ap1b, and 5-dpf larvae were live imaged for craniofacial dysmorphism (arrows) and body length quantification (G). Scale bar is 500  $\mu\text{m}$ . Error bars are SD. \*\*\*\*,  $P < 0.0001$ ; \*\*\*,  $P < 0.001$ ; two-way ANOVA with Tukey's multiple comparison test.  $n \geq 29$  mutants per condition. (H) Localization of Anpep in different  $V_0$  and  $V_1$  sector V-ATPase mutants. Arrows point to vacuolar accumulation, and arrowheads show basolateral missorting. Scale bars are 10  $\mu\text{m}$  and 2  $\mu\text{m}$  in magnified insets.  $n \geq 10$  mutants in two independent experiments per allele.



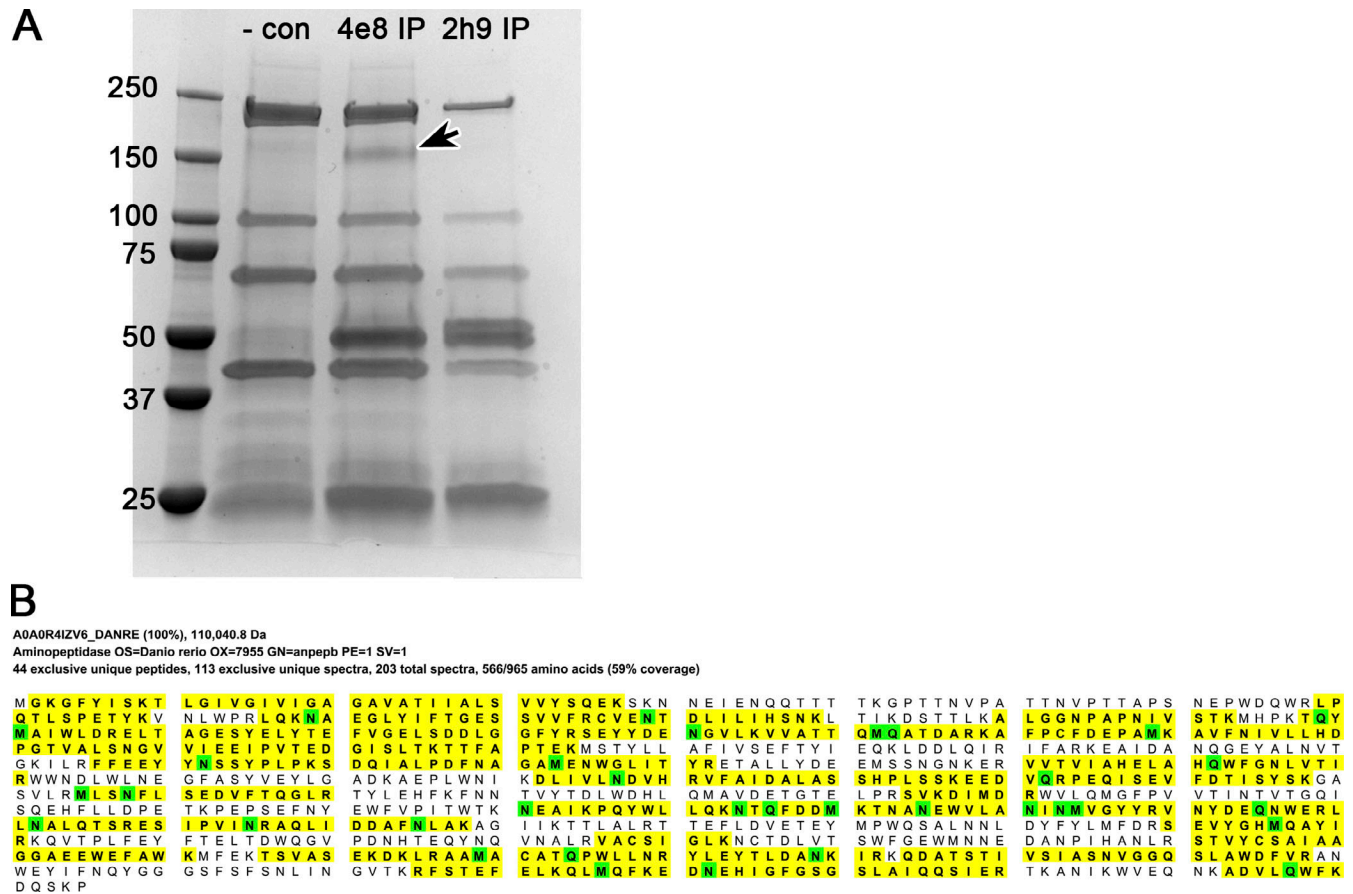


Figure S2. **Identification of Anpep as a target for the 4e8 antibody.** (A) Coomassie-stained SDS-PAGE gel of eluates from immunoprecipitation with negative control (-con; lysates incubated with Protein G agarose beads only), anti-4e8, or anti-2h9 (a different mouse monoclonal antibody used for comparison) from 5-dpf larvae. The ~150-kD band (arrow) in the Coomassie-stained gel in the 4e8 IP lane was excised and analyzed by MS. (B) Mapped MS peptides (yellow) with zebrafish Anpep (A0A0R4IZV6\_DANRE; *anpepb*, ENSDARG00000103878). Proteins were filtered at a false discovery rate <1%, with a minimum of four mapped peptides. Hits were sorted by the number of mapped exclusive unique peptide counts, leaving Anpep as the top hit with 44 exclusive unique peptides and 59% coverage. The observed molecular weight for the band in A is consistent with that of human ANPEP due to N- and O-glycosylation modifications (Naim et al., 1999).

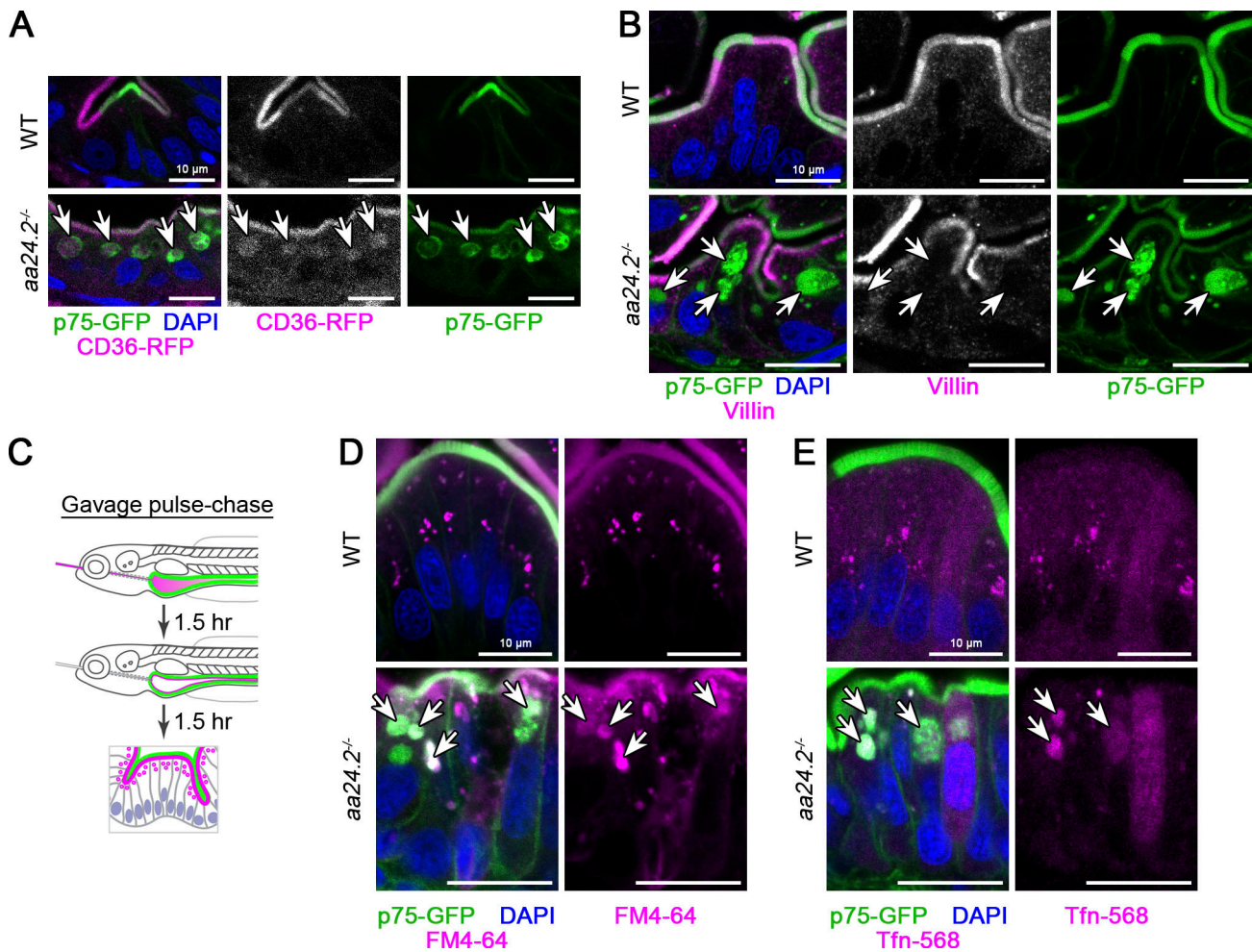


Figure S3. **Characterization of apical trafficking phenotypes in V-ATPase mutants.** (A) *aa24.2<sup>pd1209</sup>* mutants retain apical membrane proteins p75-GFP and CD36-RFP (arrows). *TgBAC(cd36-RFP)<sup>pd1203</sup>* expresses CD36-RFP at low levels in the gut, indicating that trafficking defects are not dependent on expression levels.  $n > 10$  mutants in two independent experiments. (B) *aa24.2<sup>pd1209</sup>* mutant vacuoles (arrows) do not contain MV marker villin.  $n > 10$  mutants in two independent experiments. (C) Experimental pulse-chase strategy for delivering soluble cargo to the apical surface of intestinal epithelial cells. 5-dpf larvae were gavaged with endocytic tracers and phenol red to visualize the intestinal lumen. After 1.5 h, the intestinal lumen was flushed out by gavage of excess unlabeled buffer containing no phenol red to visualize clearing of the intestine. (D and E) Internalized fluid phase FM4-64 (D) and receptor-mediated transferrin-AF568 (E) endocytic cargo accumulates in apical vacuoles (arrows) of *aa24.2<sup>pd1209</sup>* mutants. Scale bars are 10  $\mu\text{m}$ .  $n \geq 4$  mutants per condition for D and E.

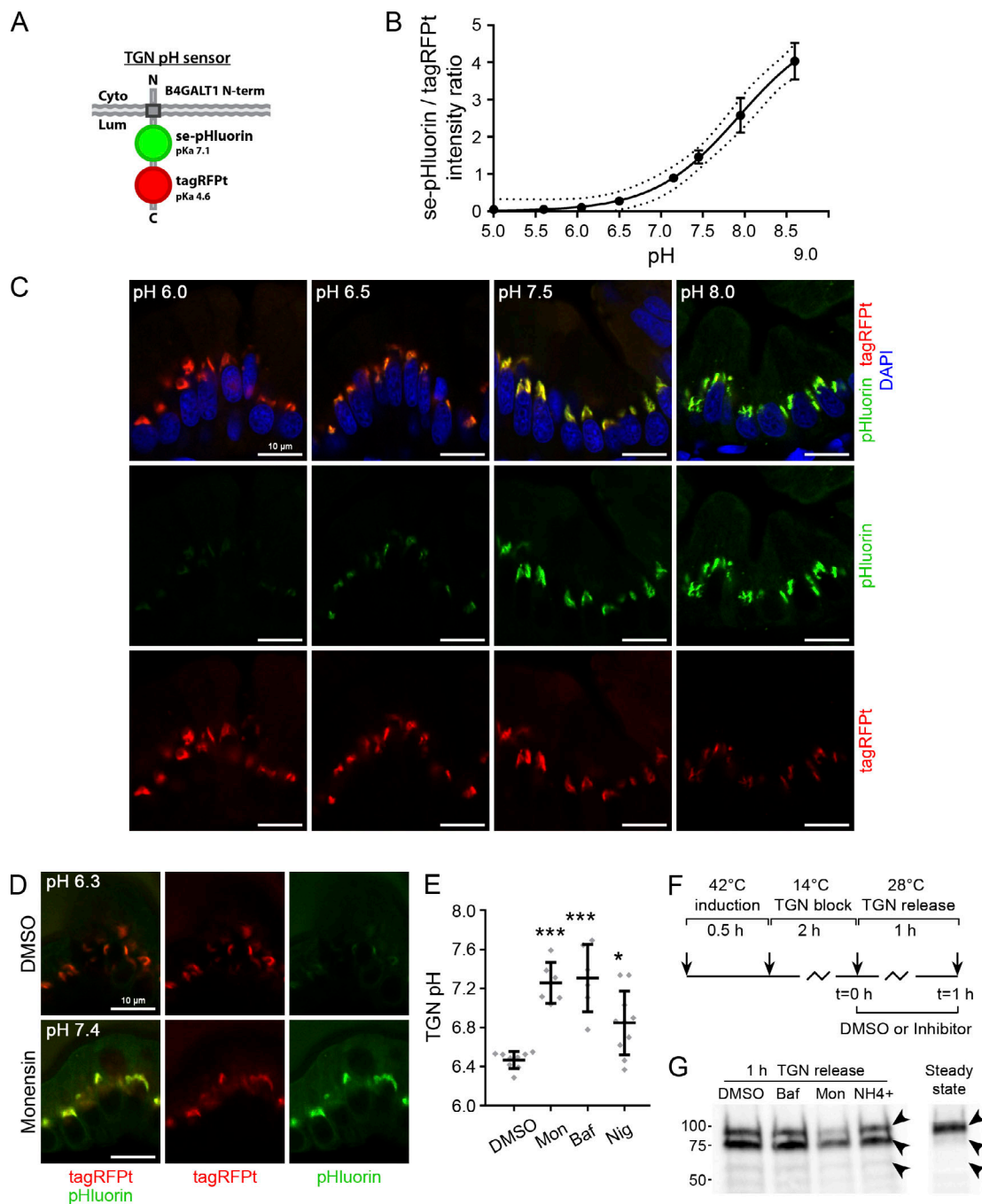
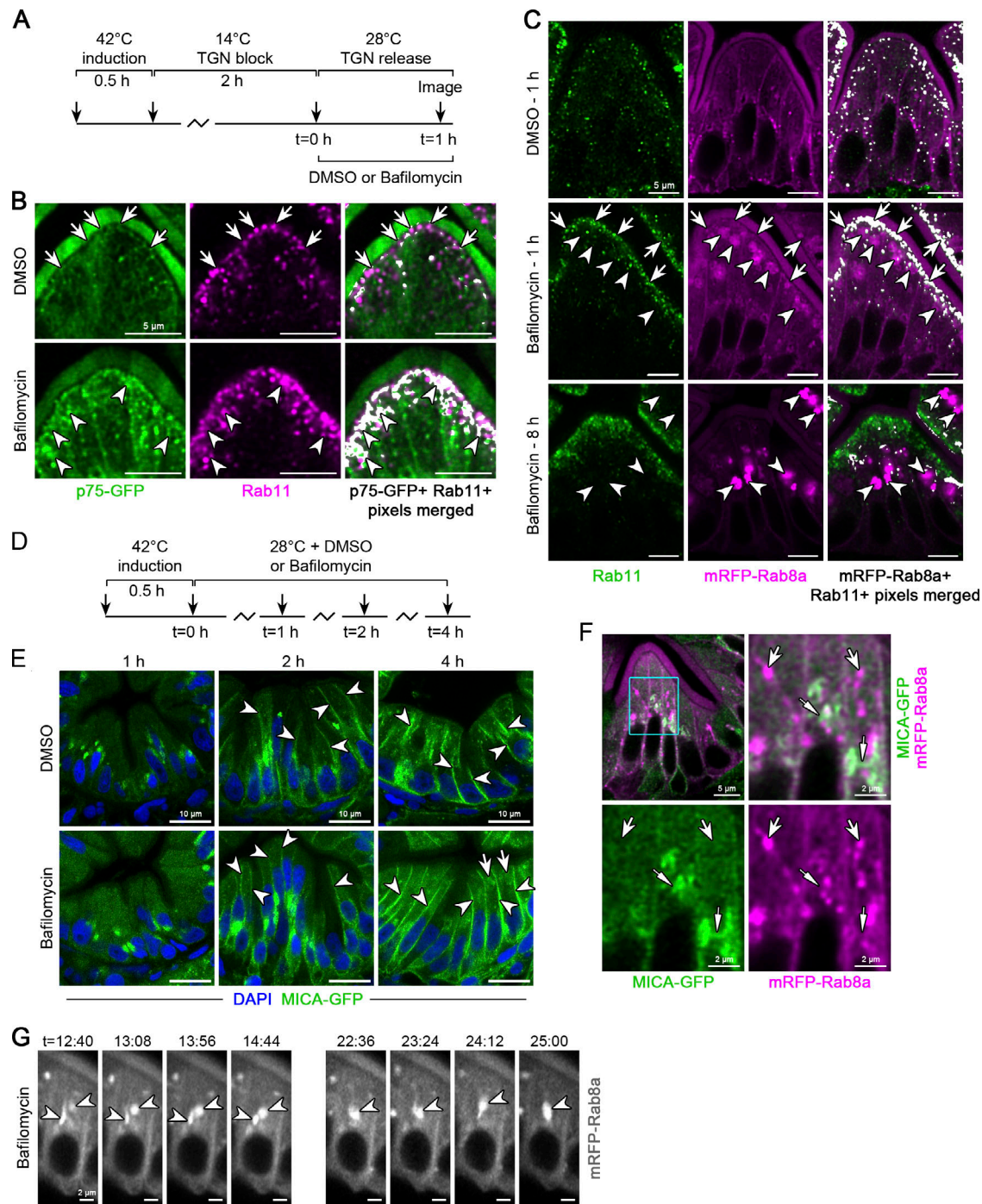


Figure S4. **Manipulation of luminal pH of the TGN and its effect on p75-GFP processing.** **(A)** Schematic structure of a luminal pH sensor for the TGN. **(B)** Calibration curve of B4GALT1-se-pHluorin-tagRFpT pH sensor. Sections of *Tg(cldn15la:qf2)<sup>pd1142</sup>;Tg(quas:B4GALT1-pHluorin-tagRFpT)<sup>pd1212</sup>* larvae were permeabilized overnight in PBS-0.5% Triton-X100 and then for 20 min in PBS-1% Triton-X100. Afterward, sections were equilibrated in pH-calibrated phosphate-citrate buffer in 20% glycerol for  $\geq 4$  h and imaged by confocal microscopy. Image acquisition parameters were set at pH 7.5 to allow high dynamic range with no saturation for each channel. All subsequent imaging for standard curve analysis and live in vivo imaging were then conducted with identical hardware and software parameters. For quantitation of ratiometric imaging of the sensor, raw 16-bit confocal data were used. Curve fitting and pH interpolation was conducted using a sigmoidal model.  $R^2 = 0.8806$ .  $n \geq 5$  animals representing  $\geq 25$  enterocytes. Error bars are 1 SEM. **(C)** Representative images from standard curve analysis from B. Scale bars are 10  $\mu$ m. **(D and E)** *Tg(cldn15la:qf2)<sup>pd1142</sup>;Tg(quas:B4GALT1-pHluorin-tagRFpT)<sup>pd1212</sup>* larvae were gavaged with 1% DMSO, 25  $\mu$ M monensin, 1  $\mu$ M bafilomycin, or 20  $\mu$ M nigericin and then allowed to recover for 1 h. Larvae were then mounted in agarose and allowed to recover from tricaine anesthesia for  $\geq 30$  min. Media were then replaced with egg water containing the same concentration of inhibitor as gavage conditions. Larvae were then live imaged with no anesthesia within 1 h later. **(D)** Representative live images. **(E)** Quantitation of TGN pH values from larvae treated with DMSO, monensin (Mon), bafilomycin (Baf), or nigericin (Nig). \*\*\*,  $P < 0.001$ ; \*,  $P < 0.05$ ; one-way ANOVA.  $n \geq 6$  animals, representing  $\geq 30$  cells. Data points are average pH values for individual animals from randomly selected TGN ROIs. Scale bars are 10  $\mu$ m. **(F and G)** Larvae expressing p75-GFP were subjected to a 1-h TGN release in the presence of 0.75% DMSO, 750 nM bafilomycin (Baf), 25  $\mu$ M monensin (Mon), or 100 mM  $\text{NH}_4^+$ . **(G)** After the 1-h treatment, p75-GFP was immunoprecipitated and analyzed by Western blot. The upper band represents the mature processed form of p75-GFP that is present at steady-state (24 h after induction). The lower bands represent immature p75-GFP intermediates.



**Figure S5. Inhibition of V-ATPase activity rapidly blocks p75 apical membrane delivery and redistributes Rab8 into vacuoles.** **(A)** Experimental scheme. **(B)** p75-GFP overlaps with Rab11 in apical tubules (arrows) and is enriched at the apical membrane in control larvae after a 1-h TGN release. Bafilomycin treatment acutely inhibits surface delivery, and p75-GFP accumulates in subcortical patches at and below the terminal web with Rab11 (arrowheads). For depiction of colocalized pixels, control and experimental larvae were processed in parallel, and identical thresholding parameters were applied using the ImageJ plugin Colocalization. Scale bars are 5  $\mu\text{m}$ .  $n = 4$  mutants. **(C)** 5-dpf larvae expressing mRFP-Rab8a were treated with DMSO or bafilomycin for the indicated times and stained for endogenous Rab11. Arrows point to accumulated mRFP-Rab8a/Rab11 signal after 1 h of bafilomycin treatment, and arrowheads show vacuoles. Scale bars are 5  $\mu\text{m}$ .  $n \geq 4$  larvae per time point. **(D)** Experimental scheme. **(E)** Biosynthetic delivery of MICA-GFP to the basolateral membrane is not significantly impacted by bafilomycin treatment. Arrowheads point to basolateral membrane signal. Arrows show small intracellular signal that begins to accumulate after 4 h of bafilomycin treatment.  $n = 3$  (1 h), 8 (2 h), or 6 (4 h) bafilomycin-treated larvae. Scale bars are 10  $\mu\text{m}$ . **(F)** MICA-GFP was imaged after a 1-h TGN release in mRFP-Rab8a expressing larvae. Wide arrows point to mRFP-Rab8a tubules lacking MICA-GFP and narrow arrows show MICA-GFP lacking mRFP-Rab8a and extending from the presumptive TGN.  $n = 12$  larvae. **(G)** 5-dpf larvae expressing mRFP-Rab8a in the gut were treated with DMSO or 1  $\mu\text{M}$  bafilomycin for 35 min and then live imaged using a Zeiss LSM 880 confocal microscope with a 40 $\times$  water immersion objective in Airyscan Fast Mode. Arrowheads show mRFP-Rab8a structures progressively collapsing to form a vacuolar-like compartment during bafilomycin treatment. See also [Video 5](#). Scale bars are 2  $\mu\text{m}$ .  $n = 6$  bafilomycin-treated larvae.

Video 1. **Live imaging of mRFP-Rab8a and p75-GFP after a 45-min TGN release.** 5-dpf larvae were subjected to a 3-h TGN block, mounted in low melting point agarose in glass-bottom dishes, and then transferred to a 28°C incubation chamber. Live imaging of the mid-intestine was started ~45 min after TGN release. Images were acquired at 1 frame/4 s. Time stamps are shown in the video. White rectangles indicate the TGN region of enterocytes.

Video 2. **Effects of V-ATPase inhibition on mRFP-Rab8a dynamics.** 5-dpf larvae were mounted in low melting point agarose in glass-bottom dishes and then covered in fresh media containing either 1% DMSO (control) or 1  $\mu$ M bafilomycin. Live imaging of the mid-intestine was started ~45–50 min after adding media. Images were acquired at 1 frame/4 s. Time stamps are shown in the video. Tracks of mRFP-Rab8 particles were assigned using mTrackJ in ImageJ.

Video 3. **Magnified inset of mRFP-Rab8a dynamics during control conditions or during V-ATPase inhibition.** This video is a magnified view of individual enterocytes from [Video 2](#). Images were acquired at 1 frame/4 s.

Video 4. **Additional examples of mRFP-Rab8a dynamics during control conditions or during V-ATPase inhibition.** Larvae were processed and imaged identically to those in [Video 2](#), but imaging was started ~60–70 min after adding media. Images were acquired at 1 frame/4 s. Time stamps are shown in the video.

Video 5. **Vacuolar collapse of mRFP-Rab8a<sup>+</sup> tubules during V-ATPase inhibition.** 5-dpf larvae were under identical conditions as used in [Videos 2, 3, and 4](#), and live imaging of the mid-intestine was started ~35 min after adding media. Images were acquired at 1 frame/4 s, and time stamps are shown in the video.